



Contents lists available at ScienceDirect

Advances in Colloid and Interface Science

journal homepage: www.elsevier.com/locate/cis

Historical Perspective

Multiphase displacement manipulated by micro/nanoparticle suspensions in porous media via microfluidic experiments: From interface science to multiphase flow patterns

Wenhai Lei, Xukang Lu, Moran Wang^{*}

Department of Engineering Mechanics, Tsinghua University, Beijing 100084, China



ARTICLE INFO

Keywords:

Particle suspension
Microfluidics
Multiphase displacement
Interface science
Wettability

ABSTRACT

Multiphase displacement in porous media can be adjusted by micro/nanoparticle suspensions, which is widespread in many scientific and industrial contexts. Direct visualization of suspension flow dynamics and corresponding multiphase patterns is crucial to understanding displacement mechanisms and eventually optimizing these processes in geological, biological, chemical, and other engineering systems. However, suspension flow inside the opaque realistic porous media makes direct observation challenging. The advances in microfluidic experiments have provided us with alternative methods to observe suspension influence on the interface and multiphase flow behaviors at high temporal and spatial resolutions. Macroscale processes are controlled by microscale interfacial behaviors, which are affected by multiple physical factors, such as particle adsorption, capillarity, and hydrodynamics. These properties exerted on the suspension flow in porous media may lead to interesting interfacial phenomena and new displacement consequences. As an underpinning science, understanding and controlling the suspension transport process from interface to flow patterns in porous media is critical for a lower operating cost to improve resource production while reducing harmful emissions and other environmental impacts. This review summarizes the basic properties of different micro/nanoparticle suspensions and the state-of-the-art microfluidic techniques for displacement research activities in porous media. Various suspension transport behaviors and displacement mechanisms explored by microfluidic experiments are comprehensively reviewed. This review is expected to boost both experimental and theoretical understanding of suspension transport and interfacial interaction processes in porous media. It also brings forward the challenges and opportunities for future research in controlling complex fluid flow in porous media for diverse applications.

1. Introduction

Multiphase displacement by micro/nanoparticle suspensions in porous media is ubiquitous in natural processes and engineering systems. Examples include but are not limited to remediation of contaminated soil and groundwater [1], geological CO₂ sequestration in deep saline aquifers or depleted oil and gas fields [2], tertiary oil recovery [3], water retention in dry soil in agriculture [4], microfluidic logic control [5], ink spreading on paper [6], and drug delivery in vascular networks [7]. In these systems, suspensions can dramatically alter the interface and multiphase flow behaviors with consequences for navigating a complex porous structure. As one of the most prominent applications, they are frequently harnessed to enhance displacement performance in geological systems. For instance, in soil remediation and enhanced oil

recovery, the nonaqueous liquid contaminants or oil trapped underground can be remobilized by injecting the suspension to overcome the in situ capillary forces and moderate the system flow heterogeneity [8,9].

Suspensions generally refer to the overall mixture in which one dispersed substance consists of microscopically insoluble particles suspended throughout another continuous substance [10,11]. In this review, to unify these particle suspension effects, micro/nanoparticle suspension is defined as the dispersed particles with approximately several nanometers to millimeters in diameter suspended in the liquid. In addition to continuous fluid displacement, such as low salinity water [12], surfactant [13], and polymer solutions [14], suspension displacement is emerging as an attractive approach to control multiphase displacement with several advantages. For example, suspensions

^{*} Corresponding author.

E-mail address: mrwang@tsinghua.edu.cn (M. Wang).

can yield good injectivity and increased displacement efficiency in low permeability porous media; endure extreme circumstances with higher or lower temperature, salinity, and pH; give rise to new interfacial phenomena and flow behaviors that can be combined with other techniques such as foam or emulsion injection. Therefore, understanding and controlling the suspension transport process to affect the macroscopic multiphase flow consequences is of key practical and economic importance.

Compared with macroscopic transport measurements in the opaque porous media, the advanced microfluidic experiments have become convenient methods for observing suspension flow dynamics and their influence on multiphase flow patterns [15,16]. Microfluidic chips, also known as micromodels, refer to transparent devices with characteristic length scales less than a millimeter for observing, handling, and manipulating fluid flow [17]. It contains several advantages, such as direct visualization, high-precision manipulating fluids, repeatable porous structure, low analysis time, and low cost [15,18]. However, limited by the materials produced for the microfluidic chip, in many cases, its solid surface properties are still difficult to realize the complex characteristics of natural porous media, and its statistical surface characteristics can only be displayed uniformly, such as uniform wettability alteration. In this review, we will only focus on the pore-scale research related to microfluidic experiments. Although pore-scale numerical simulations sometimes contain the above advantages with the development of high-performance computing, the reliability of the numerical results often needs to be verified by pore-scale experiments [19].

As a result of the characteristic length of the microfluidic system in the micrometer or nanometer scale, which is consistent with the length scale of the porous structure and particles in suspensions, interfacial phenomena governing microscopic flow physics plays a dominant role in the displacement. However, a wide gap exists from interfacial phenomena to macroscopic flow patterns and engineering application consequences. This gap is undoubtedly a complex matter influenced by many factors, such as the complex physicochemical properties of micro/nanoparticles and corresponding suspensions, the visualization and quantification of multiphase flow and suspended particles simultaneously at different scales, and underlying multi-physical phenomena of coupled suspensions with the multiphase flow.

Many suspensions have succeeded in engineering applications but sometimes also encountered various failures. The discrepancy mainly exists that micro/nanoparticles have been found to enhance the displacement in porous media [20,21], while other studies report the opposite, claiming that micro/nanoparticles will harm the flow channel and suppress the further displacement performance [22,23]. Therefore, more fundamental understandings were required to elucidate how the physicochemical properties of suspensions influence interfacial behavior and how these microscopic physics determine multiphase flow patterns and eventually achieve the best displacement.

In this review, we describe the current state-of-the-art microfluidic techniques to shed light on this puzzle from interface to multiphase flow patterns in porous media. First, we summarize the fundamentals of suspensions, such as preparation and fabrication, physicochemical property, and interfacial property. Second, developments of microfluidics, typical microfluidic materials and fabrications, and different microfluidic structure designs from purified pore structures to complex reservoir-on-a-chip are summarized. Then, the progress of microfluidic research about the effect of suspension on multiphase flow consequences in porous media was critically reviewed. Finally, we highlight new opportunities for microfluidics to explore multiphase displacement mechanisms enhanced by micro/nanoparticle suspensions in porous media, with consequences for soil or groundwater remediation, enhanced oil recovery, geological carbon sequestration, and other emerging applications.

2. Fundamentals of suspensions

Deformable and rigid particles in suspensions have been synthesized from several millimeters to nanometers for effective displacement performance in porous media. Among these dispersed systems, deformable micro/nanoparticle and rigid nanoparticle suspension have been developed as attractive agents in multiphase displacement, as shown in Fig. 1. They either have ultra-small particle sizes that can penetrate tiny pores and sub-pore scale areas where conventional fluids are difficult to reach; or are deformable and degradable to be injected into porous media without harming flow channels permanently. These suspensions contain remarkable properties, such as easy preparation, good controllability, environmental friendliness, and adaptation to complex environments [24–26]. For instance, the silica particles are similar or the same as the material in the reservoirs, and the microgel particles can be degraded in the formation due to high temperature or long-term flooding, which is easier to handle and has little impact on the environment.

Fig. 1A–C presents three typical deformable micro/nanoparticles: preformed particle gel (PPG) at the millimeter scale, microgel particle at the micron scale, and nano-hydrogel at the nanometer scale. Deformable particles are a chemically crosslinked network of polymer chains swollen in a solvent. The size of deformable particles can be comparable to the pore size of the porous medium (order-of-magnitude range $\approx 10^1 \sim 10^2 \mu\text{m}$). Some studies also synthesized nano-hydrogel particles for improving displacement performance in the ultra-low permeability porous media [27,28]. The particle plugging, particle-concentration-manipulated rheology, and adhesion effect will influence the multiphase flow behaviors. Fig. 1D–F presents three typical rigid nanoparticles: zero-dimensional silica nanoparticles, one-dimensional carbon nanotube, and two-dimensional graphene oxide. Different morphology and materials will present different thermodynamic properties and influence the interfacial phenomena. For example, graphene or graphene oxide nanoplatelets contain extensive surface area per mass and unique properties, including very high electrical and thermal conductivities and good mechanical properties [29]. Rigid nanoparticles are much smaller than the pore size, and they are defined as characteristic particle sizes ranging from 1 to 100 nm [30]. Their excellent capacity with the spreading, adhesion, and self-assembly properties may enhance the interfacial phenomena, which affect the multiphase flow patterns and final displacement consequences.

Besides, natural geological particles such as clays and other fine materials sometimes can be equally impactful to multiphase flow in porous media as the above artificial particulate systems [31]. Clay or fines migration may damage formation, potentially, decreases in porous media permeability significantly and, hence, the displacement efficiency of defending phase from reservoirs [32]. However, it can be combined with low salinity brine injection, which may overcome this harmful behavior and promote defending phase flow. Meanwhile, spontaneous Pickering emulsification by clay in clay-rich formation will promote flow diversion in preferential flow paths [33,34]. Pore plugging particles or emulsions in water-filled pores obstructed preferential flow paths and diverted injection fluid to unswept regions thereby increasing displacement efficiency [35].

In this section, we will introduce the synthesis and preparation of these artificial particle suspension systems, then microscopic particle kinetics of these suspensions are summarized and classified as particle aggregation and dispersion kinetics, particle adsorption kinetics, particle ordering kinetics in the thin film, and particle deformation and transport kinetics. Finally, macroscopic suspension properties, such as interfacial tension, wettability, rheology, and elastic modulus and strength, are concluded. These microscopic particle kinetics and macroscopic suspension properties, alone or in combination, can affect subsequent multiphase flow patterns. For example, particle diffusion can be combined with fluid rheology to describe the concentration-manipulated rheology controlling multiphase flow patterns [36], and

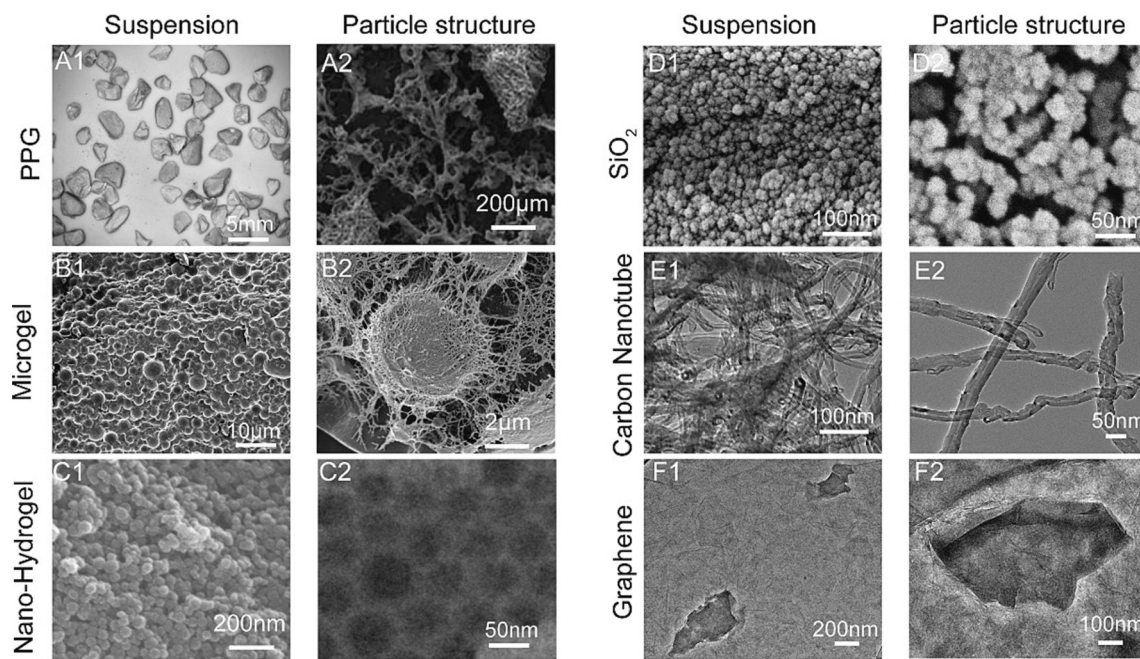


Fig. 1. The morphology of (A–C) deformable micro/nanoparticle suspension and (D–E) rigid nanoparticle suspension. (A1) Performed particle gel (PPG) suspension and (A2) PPG particle structure. Fig. A2 is from Li et al. [38]. (B1) Microgel particle suspension and (B2) microgel particle structure. (C1) Nano-hydrogel suspension and (C2) Nano-hydrogel structure. Fig. C2 is from Li et al. [28]. (D1) Silica nanoparticle suspension and silica nanoparticle structure. (E1) Carbon nanotube suspension and (E2) carbon nanotube structure. (F1) Graphene oxide suspension and (F2) graphene oxide structure.

particle instability in the suspension may induce unique multiple particles plugging and squeezing through porous media, which affects the preferential flow pathway during multiphase displacement [37].

2.1. Synthesis and preparation

2.1.1. Deformable particle suspension

The inverse suspension polymerization methods [28,36,39,40] were widely used to make micron- or nanoscale deformable particles. The main idea of this synthesis method was to use the oleic phase as the continuous phase and disperse the monomer aqueous solution into several reactive microdomains stabilized using surfactants to prepare deformable particles. The stock deformable particle suspension was commonly synthesized by the following materials: acrylamide, water-soluble monomer, dispersion stabilizer (surfactant), oleic solvents, and aqueous phase. Then deformable particle suspensions used in applications were prepared by diluting the stock deformable particle suspension with an aqueous phase to achieve the desired injection concentration.

The mechanical shearing or grinding method [41–43] is one of the earliest methods for deformable particles, which was commonly prepared from bulk gel. First, the bulk gel was formed by making the aqueous solution containing acrylamide, crosslinker, initiator, and other additives. Then the bulk gel was sheared or cut into small particles or pieces. Sometimes, these two steps can be combined by applying the shear rate during the crosslinking process in a Couette geometry or a well-defined porous media by injecting at a constant flow rate [41]. Finally, deformable particle suspension can be achieved by dispersing these particles into the aqueous liquid.

2.1.2. Rigid nanoparticle suspension

Three typical materials: silica, metal oxide, and carbon, are used to synthesize the rigid nanoparticles. Silica nanoparticles are cost less and environmentally friendly than other materials. Silica sols and fumed silica are the primary materials to fabricate nanoparticle suspension for multiphase displacement. Silica sols are usually prepared in sodium silicate solutions by ion exchange [44], which can maintain stability under very high particle concentrations. Particles are formed from the

silica nuclei, and the corresponding particle size depends on polymerization conditions, which vary from less than 5 nm to about 100 nm. Fumed silica is synthesized by the pyrolysis method, in which silicon tetrachloride reacts with oxygen in a flame under high temperature, and the silica particles gradually grow in size [45]. The final state of fumed silica is usually branched agglomerates of the primary particles with an average size larger than 150 nm [46].

Metal oxide nanoparticles, such as aluminum oxide (Al_2O_3), iron oxide (Fe_2O_3), nickel oxide (NiO_2), and zirconium oxide (ZrO_2), can be synthesized using many different methods [47]. Solution-based methods, such as sonochemical, solvothermal, sol-gel, and micro-emulsion, are popularly accepted in fabrications. The other is vapor-phase methods such as laser ablation, combustion, and template/surface-mediated synthesis. These methods in different fabrication conditions can determine the shape and size distribution of these nanoparticles. Thus, it is possible for a specific design for interfacial and flow properties.

Carbon materials such as graphene, carbon nanotube, and fullerene have attracted more attention due to their excellent interfacial properties [48]. The main techniques for synthesizing carbon-based nanoparticles are chemical vapor deposition (CVD) and arc discharge. Surface functionalization is usually involved in increasing their hydrophilicity by adding functional groups such as carboxyl and hydroxyl groups due to the hydrophobicity of these materials. Graphene oxide (GO), which is the product of the chemical exfoliation of graphite using the modified Hummer's method [49], are the most widely used carbon materials due to its natural amphiphilicity [50].

2.2. Microscopic particle kinetics

2.2.1. Particle aggregation and dispersion kinetics

2.2.1.1. Pure particle suspension. The aggregation and dispersion kinetics of pure particle suspension depends on the effective form of the system interaction energy, that is, the sum of free energy W as a function of the separation distance h of the particles $W(h) = W_{VDW}(h) + W_{EDL}(h)$

+ $W_s(h)$ [51]. Interparticle behavior results from intermolecular and surface forces, e.g., van der Waals (VDW) force, the repulsive electrostatic double layer (EDL), and structural force [52]. Interparticle forces present in suspension were estimated using the extended Deryagin-Landau-Verwey-Overbeek (DLVO) theory. The balance of these forces determines particle aggregation or dispersion state.

The van der Waals force $P_{VDW} = -\partial W_{VDW}/\partial h$ dominates when the particle distance h is small. The van der Waals interaction usually originates from the dipole-dipole, dipole-induced-dipole, and dispersion forces, $W_{VDW} = -A/(12\pi h^2)$, where A is the Hamaker constant of Materials 1 and 2 separated by Material 3 [53–55]. $A = A_{v=0} + A_{v>0} =$

$$\frac{3k_B T}{4} \left(\frac{\epsilon_1 - \epsilon_3}{\epsilon_1 + \epsilon_3} \right) \left(\frac{\epsilon_2 - \epsilon_3}{\epsilon_2 + \epsilon_3} \right) + \frac{3h_p \nu_e}{8\sqrt{2}} \frac{(n_1^2 - n_2^2)(n_2^2 - n_3^2)}{(n_1^2 + n_2^2)^{1/2} (n_2^2 + n_3^2)^{1/2} \{ (n_1^2 + n_2^2)^{1/2} + (n_2^2 + n_3^2)^{1/2} \}}$$

where k_B is the Boltzmann constant, T is the Kelvin temperature, ϵ_i is the zero-frequency dielectric constant of phase i , h_p is Planck constant, ν_e is the electronic absorption or ionization frequency and n_i is the refractive index. The first term $A_{v=0}$ is a zero-frequency term resulting from the dipole-dipole and dipole-induced-dipole forces of polar molecules, while the second term $A_{v>0}$ is a high-frequency term resulting from the dispersion forces. For a pure component, the zero-frequency term is usually much smaller than the high-frequency term. However, for the multi-component system described here, the zero-frequency term will become important and the relative magnitude should be carefully evaluated to determine whether any term could be ignored. Another important factor for surface interaction in a liquid medium is the distance-dependence of the van der Waals energy, which is known as the retardation effect due to the limited speed of transmission of electromagnetic waves. It is only the dispersion energy that suffers retardation while the zero-frequency orientation and induction energies remain nonretarded at all separations. However, the zero-frequency contribution, which is essentially an electrostatic interaction, will suffer screening effects in electrolyte solution with an exponentially decay term [10].

The surface geometry can highly impact the expression for the van der Waals interaction [56]. The general equation for non-retarded van der Waals interaction between identical particles is $W_{VDW}(h) = -A/6 \left[\frac{2r^2}{(4r+h)h} + \frac{2r^2}{(2r+h)^2} + \ln \left(\frac{4r+h}{2r+h} \right) \right]$, which is valid at all separations [57]. The Derjaguin approximation [58] is commonly used which gives $W_{VDW}(h) = -A/(6rh)$ for identical particles, where r is the particle radius and h is the film thickness. However, the premise of the Derjaguin approximation is that the distance between particles is much smaller than the particle size, thereby reducing spherical surfaces to infinitesimally parallel rings each of which can be considered as a flat plate. Therefore, for nanoparticles, the Derjaguin approximation becomes very inaccurate since particle size is comparable to particle distance. Surface element integration (SEI) is another newly developed approximation for curved or rough surfaces, which overcomes some drawbacks of the Derjaguin approximation [59–62].

The charged surface attracts counter-ions and repels co-ions, which leads to a totally different ion distribution near the interface. The electrical potential distribution in the diffuse layer is governed by the Poisson–Boltzmann equation (PBE). For two charged surfaces, the electrical potential distribution in 1D can be analytically solved under the Debye-Huckel approximation for a 1:1 electrolyte. The Debye-Huckel approximation approximates the exponential term with a linearized one, which is only valid when $|\frac{z_i e \phi}{k_B T}| < 1$, or for systems having low surface charges with potentials approximately less than 25 mV at 25 °C, where z_i is the number of charges carried by the ion, ϕ is the electrical potential and e is the elementary charge.

Based on the electrical potential distribution, the EDL interaction energy can be derived by three methods. The surface charging method and the electrolyte discharging method apply assumed reversible processes to calculate the free energy, while the pressure integrating method uses thermodynamic relations to analyze the pressure between

charged surfaces. An important influencing parameter determining the expression for EDL interaction is the boundary condition, which includes the CP-CP, CC-CC and CR boundaries. The constant potential (CP) and the constant charge (CC) boundary conditions are most widely used to simplify the problem. For a 1:1 electrolyte with Debye-Huckel approximation, the Hogg-Healy-Fuerstenau (HHF) equation (*Mutual Coagulation of Colloidal Dispersions*, Hogg, 1965) for the EDL interaction energy, $W_{EDL}(h) = \frac{\epsilon \epsilon_w k [2\zeta_1 \zeta_2 - (\zeta_1^2 + \zeta_2^2) e^{-\kappa h}]}{2 \sinh(\kappa h)}$, can be derived by applying the CP-CP boundary, where ζ_1 and ζ_2 are the ζ -potential of surface 1 and surface 2, respectively. $\kappa^{-1} = \sqrt{(\epsilon \epsilon_0 K_B T)/(2N_A e^2 I)}$ is the Debye length, wherein $I = 0.5 \sum z_i^2 \rho_i$ is the ionic strength, ρ_i is the ion concentration (mol/kg). When the two EDLs are weakly overlapped, linear superposition approximation (LSA) gives $W_{EDL}(h) = 64k_B T n^\infty \tanh^2 \left(\frac{e\zeta}{4k_B T} \right) \exp(-\kappa h)/\kappa$ for a 1:1 electrolyte also under the CP-CP boundary, where n^∞ is the number density of ions in the bulk solution. The LSA solution can be used for conditions with higher zeta potentials, but invalid when the EDLs are strongly overlapped. Moreover, it can only work for identical or similar surfaces. It should be noted that simplified boundary conditions may lead to great errors for thin films. When the sum of the net surface charges is not zero, the CC-CC boundary would lead to infinite zeta potentials, and may produce unphysical EDL repulsion between oppositely charged interfaces. Similarly, when the zeta potentials of the two surfaces are not equal, the CP-CP boundary would lead to infinite surface charge densities, and may produce unphysical EDL attraction between identically charged interfaces. In practice, if the zeta potentials of the surfaces differ very little, a safe approach is to take the mean of the two, $\zeta = (\zeta_1 + \zeta_2)/2$, and substitute them into the HHF equation [63]. In realistic conditions, the interface charging quantities of the two surfaces would interact with each other, which is called charge regulation (CR). The CR boundary solves the potentials and the charge densities using four equations based on electrostatic equilibrium conditions and charging models of the two surfaces. This boundary condition is more physically realistic and safer to use, but complex to solve [63].

Similarly with the van der Waals interaction, for identical spherical colloidal particles, the EDL interaction when applying Derjaguin approximation becomes $W_{EDL}(h) = \pi \epsilon \epsilon_w r (\zeta_1^2 + \zeta_2^2) \left[\frac{2\zeta_1 \zeta_2}{(\zeta_1^2 + \zeta_2^2)} \ln \left(\frac{1 + \exp(-\kappa h)}{1 - \exp(-\kappa h)} \right) + \ln(1 - \exp(-\kappa h)) \right]$ under constant potential condition [54,64]. For $\zeta_1 = \zeta_2 = \zeta$, it becomes $W_{EDL}(h) = 2\pi \epsilon \epsilon_w r \zeta^2 \ln(1 + \exp(-\kappa h))$. It should be noted that the above expression is only valid when the double layer thickness is much smaller than the particle size (at least $\kappa r > 5$) and the zeta potential is small (Debye-Huckel approximation). LSA is also commonly used to derive the expression for spherical interactions, which gives $W_{EDL}(h) = 64\pi \epsilon \epsilon_0 \left(\frac{k_B T}{e} \right)^2 \frac{r^2}{h+2r} \tanh^2 \left(\frac{e\zeta}{4k_B T} \right) \exp(-\kappa h)$ [65], valid for small zeta potential and all κr provided that κh is large enough. Linear superposition approximation is more commonly used to derive the expression for spherical interactions, which gives $W_{EDL}(h) = 4\pi \epsilon \epsilon_0 \frac{r^2}{h+2r} \zeta^2 \exp(-\kappa h)$. For thin double layers, we have $W_{EDL}(h) = 32\pi \epsilon \epsilon_0 r \tanh^2 \left(\frac{1}{4} \zeta \right) \exp(-\kappa h)$ [65]. A more detailed comparison of the Derjaguin approximation, linear superposition approximation and surface element integration can be found in the work by Bhattacharjee et al. [66].

The general trend of DLVO interactions in the nanoparticle suspension are shown in Fig. 2A. The DLVO theory is classic and very useful for describing the stability of commonly encountered suspension systems, but for special conditions, the applicability needs to be carefully evaluated. For instance, when particle concentration is too high, pair-pair interaction may be invalid for describing the multi-body interactions. The non-uniform distribution of particles and solvents due to flow in porous media and also the polydispersity means the identical values for particle size, Debye length or zeta potential may not be suitable.

The structural force is a general term for relatively short-range in-

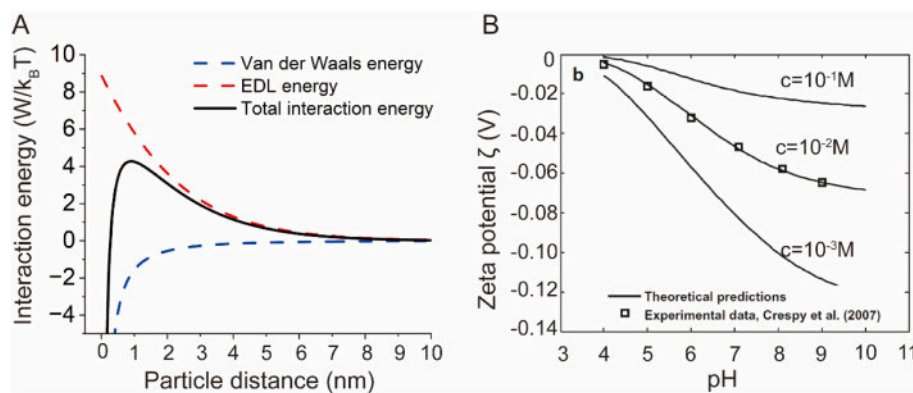


Fig. 2. (A) The general trend of DLVO interactions in the nanoparticle suspension. (Silicon (IV) oxide in water (Alfa Aesar) was diluted with deionized (DI) water to 4 wt% with a nominal (geometric) diameter of 20 nm and the ionic strength is about 0.03 M). (B) Theoretical predictions and experimental data for the silica surfaces interacting with NaCl solution, zeta potential as a function of pH for three different NaCl concentrations. The data are from Wang and Revil [73].

teractions that cannot be described by the DLVO theory when the distance is extremely small [67]. It is often called the solvation force when the medium is a solvent and the hydration force if the solvent is water. The microscopic interpretation of the structural force is basically the polar interactions including the effects of hydrogen bonding and specific ion-water interactions, which can be designated as Lewis acid-base or electron-acceptor/electron-donor interactions [68,69]. The structural energy is usually calculated from the following expression $W_s(h) = h_s A_s e^{-\frac{h}{\lambda_s}}$, where h_s and A_s can be obtained empirically [36]. In fact, the theory of surface tension components has demonstrated the additivity of the Lifshitz-van der Waals and the polar surface tension components and the non-additivity of electron-acceptor/electron-donor components. The modified Young-Good-Girifalco-Fowkes equation [70,71] gives $(1 + \cos \theta) \sigma_L^{TOT} = 2 \left[(\sigma_S^{LW} \sigma_L^{LW})^{\frac{1}{2}} + (\sigma_S^+ \sigma_L^-)^{\frac{1}{2}} + (\sigma_S^- \sigma_L^+)^{\frac{1}{2}} \right]$, where the subscripts S and L stand for solid and liquid, the superscript LW stands for Lifshitz-van der Waals interfacial tension, + and - stand for electron-acceptor and electron-donor respectively. The relation between contact angles and the unknown controlling parameters of polar liquid can be determined by means of contact angle measurements with three different liquids.

When rigid nanoparticles are dispersed in the aqueous fluid, electrostatic stabilization is the fundamental approach to increasing EDL force to overcome particle aggregation due to VDW force. The ionic strength of the suspensions determines the Debye length, which represents the radial size of the diffuse layer at the particle surface. Low ionic strength contributes to a large ion cloud extending far from the particle surface, repelling particle-particle aggregation. However, high ionic strength (e.g., high salinity water) compresses the EDL length, destabilizing nanoparticle suspensions [72]. Another critical factor is the zeta potential, which is affected by ion concentration and pH, as shown in Fig. 2B. Basically, the larger the net zeta potential, the more stable the suspension [73]. As salt concentration increases, the Debye length will decrease due to compression of the double layer. The Huckel limit and the Smoluchowski limit corresponds to $kr \ll 1$ for smaller particles at low salt concentrations and $kr \gg 1$ for larger particles at high salt concentrations, respectively. When applying electrophoresis to measure the zeta potential, the double layer thickness will highly impact the force balance and the motion of the particles, and the expressions for zeta potential will be quite different under different limits. For example, the silica-NaCl aqueous fluid interface is more negatively charged for higher pH and lower concentration, stabilizing silica nanoparticle suspensions [63,72–74]. It is worthy to note that the silanol group may become positively charged by accepting protons under very acidic solutions ($pH < 3$), and the silica significantly dissolves into silicate ions $HSiO_3^-$ in basic solution ($pH > 9$) [73].

The extended DLVO force plays an important role not only in the

stability of suspensions but also in the adsorption of particles on solid walls and the formation, evolution, and flow of microscopic fluid films, such as capillary condensation on nano rough surfaces, electroosmotic flow in nanochannels, etc. All these effects may affect the multiphase displacement consequences, which will be introduced and discussed in Section 2.2.2.

In addition to the extended DLVO forces, macromolecules (such as polymer) particles or adsorption of nonionic macromolecules onto the surface of particles can lead to the steric force [75]. The steric force contains the long-range osmotic pressure and the relatively short-range elastic recoil force [51]. At small separations, the elastic compression of anchored chains dominates the attractive van der Waals force and the total interaction potential actually exhibits no minimum at contact, which is different from pure colloidal interactions. The colloidal suspension is thermodynamically stable if the layer is thick enough and the polymeric chains do not desorb. Instability occurs at a separation comparable to the layer thickness due to the polymer-polymer interactions or particle-particle attractions acting across thin layers. The theoretical model for interaction potential between spheres with polymer layers has been well-established and a well-defined critical flocculation point exists and varies under different conditions [54]. Steric force is commonly encountered in suspension with polymer particles [76]. The magnitude of the steric force depends on the grafting density of macromolecules on the particle surface and their interaction with the fluid. By comparing microgel particles with different contents of crosslinker, it has been demonstrated that increasing the degree of crosslinking increases the aggregation of particles [77]. It has also been shown that the combined electro-steric repulsion using charged macromolecules can decrease suspension aggregation [78]. Besides, non-adsorbing polymers, as an important additive in multiphase displacement process, have also been combined with particle suspensions. When non-adsorbing polymers exist freely in the bulk solution, the depletion force between relatively large particles will arise and influence colloidal stability. The depletion force is an attractive force arises between colloidal particles in a dilute solution of depletants [79]. The non-adsorbing polymers, as the depletants, are preferentially excluded from the vicinity of the particles since the total entropy of the system will increase accordingly. The depletion force can lead to the flocculation of the colloids, which should be carefully evaluated when non-adsorbing polymers exist in particle suspensions [80].

2.2.1.2. Compound particle suspension. When the stock microgel particle suspension is prepared by the inverse suspension polymerization method and diluted in water to a specified concentration, most microgel particles will disperse from the droplet of the stock suspension, while some microgel particles may still be trapped within the oleic droplet as particle clusters, called microgel-in-oil. This new compound particle was

discovered and synthesized as high-performance displacement additives in multiphase flow in porous media [81–83]. The formation process of microgel-in-oil in the suspension is illustrated in Fig. 3A. Cryo-SEM of the stock microgel particle suspension and the diluted microgel particle suspension at various magnifications are presented in Fig. 3B. The microgel particles are well-dispersed in the stock microgel particle suspension, and their particle size is relatively uniform. However, in the aqueous diluted microgel particle suspension, microgel-in-oil appears aggregated with several times a single microgel particle diameter. Under higher magnification, the internal structure of microgel particles can be observed, where a porous interconnected network of polymer chains forms the spherical particle (Fig. 3B). Their aggregation and dispersion kinetics differ from the pure particle suspension [84]. Different microgel-in-oil content will influence the suspension transport modes, affecting displacement efficiency.

The aggregation state as microgel-in-oil or the dispersion state as plain microgel particles are determined by oil content and the surfactant [81–83]. The interactions between the particles and the fluid–fluid interface, interactions between particles, and the thermal energy of the system determine what particle state is formed [85]. Applying the demulsifier or ultrasound can transfer the microgel-in-oil into plain microgel particles [36]. Fluorescence microscope observations on the suspension formation process are shown in Fig. 3C. Most microgel

particles were initially entrapped in oil droplets, then particles were released from the oil droplets rapidly and soon reached stability after 200 s. Some particles were still trapped in oil droplets during the dilution process. The fluorescence microscope micrographs of the microgel particle suspension with 1 vol% particle concentration in the absence and presence of 2 wt% demulsifiers (Sulfo betaine 12, S12) are presented in Fig. 3D. It is evident that the addition of S12 makes many microgel-in-oil decompose into well-dispersed particles, and microgel-in-oil content is significantly reduced.

2.2.2. Particle adsorption kinetics

2.2.2.1. Adsorption at the fluid–fluid interface.

The phenomenon that particles can reside at the fluid–fluid interface, providing them with resistance against interface coalescence or fusion, coarsening or Ostwald ripening of droplets and emulsions, which is known as Pickering stabilization and has been demonstrated well using different methods types of particles [86]. Emulsions stabilized by solid particles are known as Pickering emulsions, where the particles have a strong tendency to adsorb or assemble at liquid–liquid interfaces. In a given Pickering emulsion system, a decrease in the interfacial energy is related to the particle size, $\Delta E = -\pi R^2/\gamma_{ow}[\gamma_{ow} - (\gamma_{wp} - \gamma_{op})]^2$, where R is the solid particle radius, and γ_{ow} , γ_{op} and γ_{wp} represent the interfacial tension of

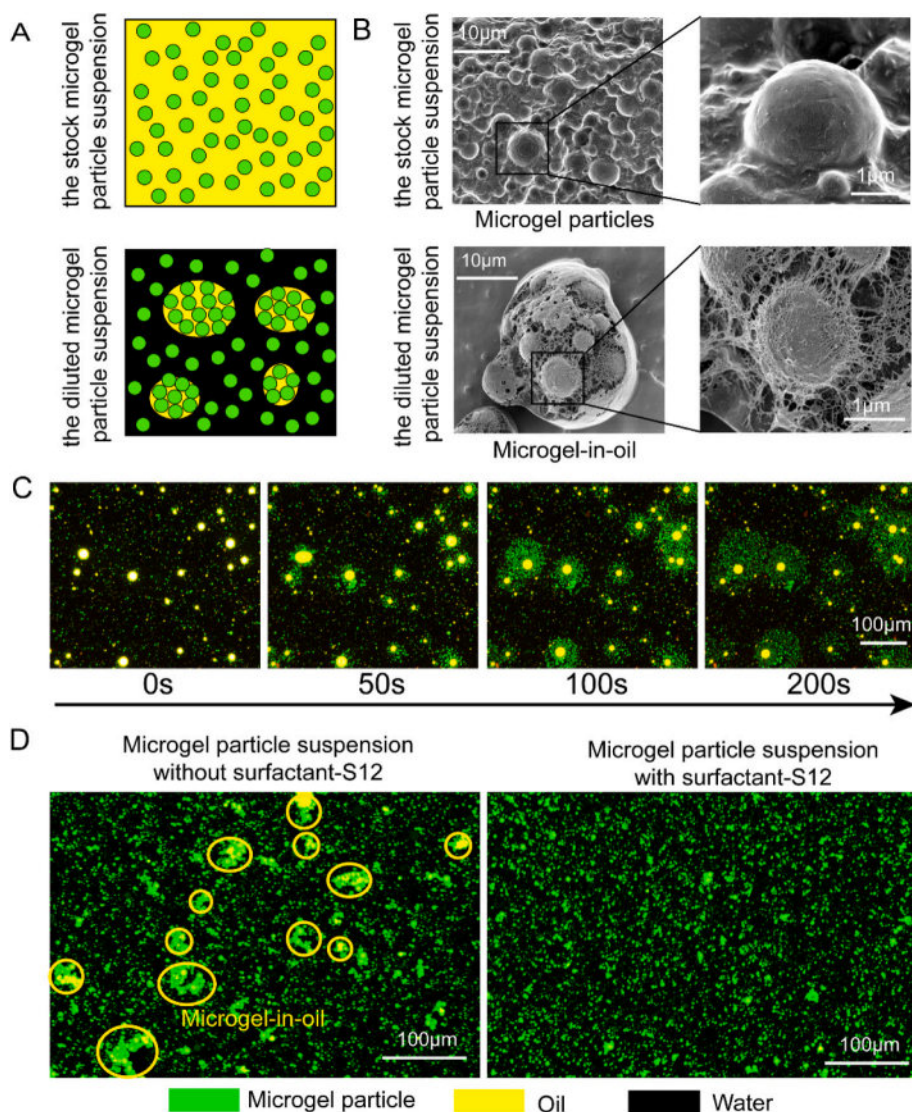


Fig. 3. (A) Schematic of microgel-in-oil formation by diluting the stock microgel particle suspension in water. (B) Cryo-SEM micrographs of the stock microgel particle suspension (up) and the diluted microgel particle suspension (down), showing the external structure (left) and local view of microgel particles (right), respectively. (C) The formation process of the microgel particle suspension. The stock microgel particle suspension in the oleic phase was dispersed in water, and the particles were released from the oil droplets within 200 s. (D) The fluorescence micrographs of microgel particle suspensions in the presence or absence of microgel-in-oil can be controlled by the surfactant-S12. Figures are from Lei et al. [37].

oil-water, oil-particle, and water-particle respectively. Rigid particles absorbed in the fluid–fluid interface obey the Young-Dupre relation $\gamma_{ow} \cos \theta + \gamma_{wp} = \gamma_{op}$, where θ is the contact angle between the particle surface and oil-water interface on the waterside, which is determined by γ_{ow} , γ_{op} and γ_{wp} (Fig. 4A). The adhesion energy of the rigid particle is described as $\Delta E = \pi R^2 \gamma_{ow} (1 \pm \cos \theta)^2$, which equals the escape energy needed to remove the particle from the interface into either the water phase or oil phase [87]. For the contact angle $< 90^\circ$ (relatively hydrophilic), the particle is more easily removed into the water phase, and the reverse is valid for the contact angle $> 90^\circ$ (relatively hydrophobic).

Deformable particles can be better emulsifiers or fluid–fluid interface stabilizers than hard particles because they stretch at fluid interfaces [88]. The deformation of a particle at a fluid–fluid interface is governed by the competition between bulk elasticity and interfacial tension [89]. Considering an extreme case of perfectly-soft particles, adsorption of perfectly-soft particles take a lenticular shape, given by Neumann’s triangle construction. This deformation can increase adsorption energies by magnitude relative to rigid particles, as shown in Fig. 4 A and B. The adsorption energies ratio of soft-particle to hard-particle $\Delta E_{soft}/\Delta E_{rigid}$ depends on γ_{op}/γ_{ow} and γ_{wp}/γ_{ow} (Fig. 4C). Considering an ideal case about neutrally wettability particles with the same interface tension in oil and water ($\cos \theta = 0$, $\gamma_{op} = \gamma_{wp} = \gamma_p$), the adsorption energy of the deformable particle is $\Delta E_{soft} = \pi R^2 \gamma_{ow} + \pi R u_r(R, \pi/2)$, where u_r is the r-direction displacement in the spherical coordinates (r, θ, ϕ), the first term $\pi R^2 \gamma_{ow}$ is the adsorption energy of a rigid particle ΔE_{rigid} , and the second term $\pi R u_r(R, \pi/2)$ is the energy change due to particle stretching, detailed calculation can refer to Style et al. [90]. The adsorption energy

depends on RE/γ_p and γ_p/γ_{ow} , where E is elastic modulus of soft particles. A transition from perfectly soft to rigid behavior of particles will happen with the increase of RE/γ_p and adsorption energy increases with decreasing γ_p/γ_{ow} [90], as shown in Fig. 4D.

Interfacial self-assembly of micro/nanoparticles can also occur and affect multiphase flow patterns during displacement processes, which is commonly encountered in the procedure of preparing large-scale nanoparticle monolayers [91,92]. The Marangoni effect is important to fabricate highly reproducible particle monolayers due to particles could be easily transferred and compressed along the fluid–fluid interface due to the interfacial tension gradient.

2.2.2.2. Adsorption at the fluid–solid interface. Adsorption of micro/nanoparticles onto solid surfaces can change solid surface properties to affect the transport behavior of suspensions and defending phase mobility in porous media. The particle adsorption is mainly controlled by the surface charge of particles and solid substrates, pH, salinity, temperature, and particle concentration. The coupling of physical, electrostatic, and hydrogen bonding adsorptions determines the final particle adsorption consequences [93]. Generally, electrostatic adsorption dominates the adsorption process when the negatively charged particle meets positively charged substrates [93–95]. For example, the surface charge of silica or metal oxide nanoparticles are negative, which is easier absorbed on some calcite surface with positive charges; positively charged polystyrene particles are easier absorbed on the negatively charged glass surface due to strong electrostatic attraction [96]. Repulsive particle interactions that predominate in some systems may

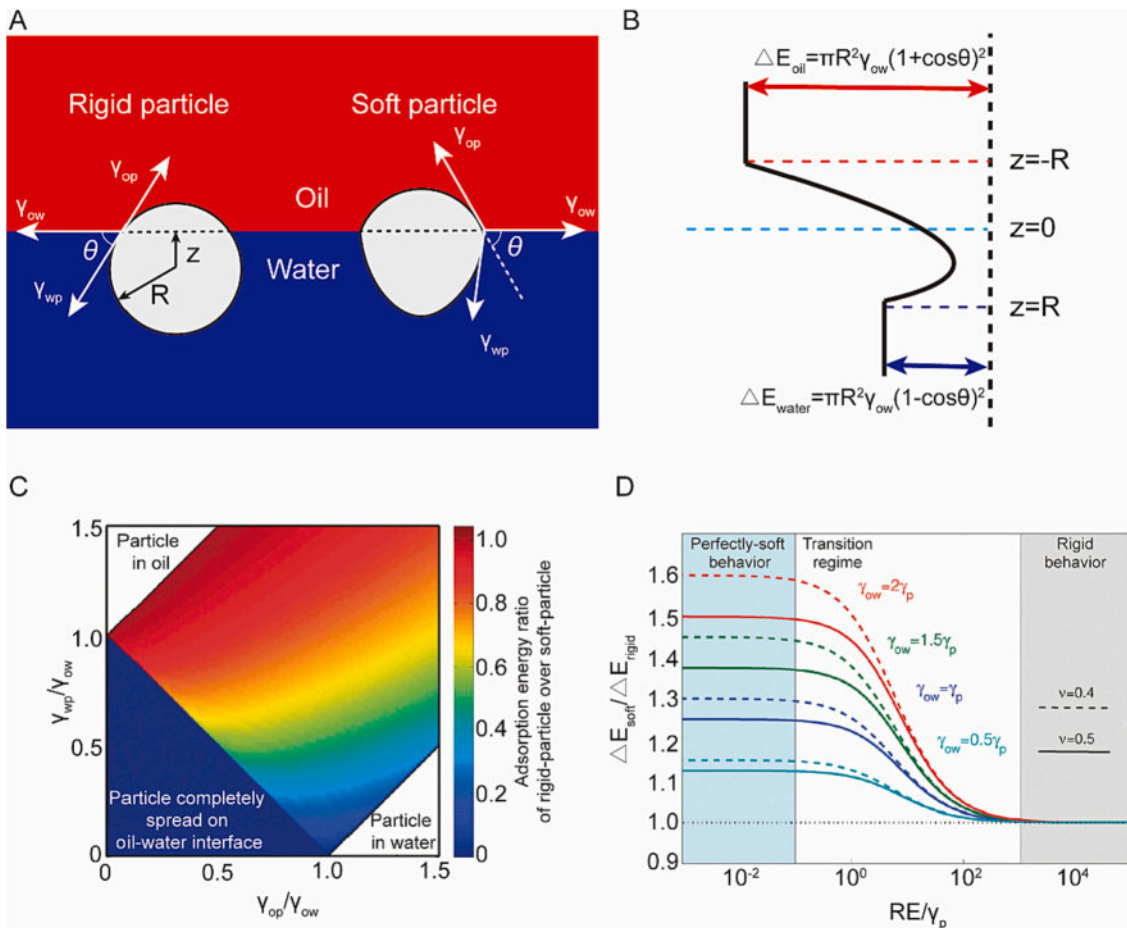


Fig. 4. Schematic representation of (A) force analysis about rigid and deformable particles absorbing at the water-oil interface, and (B) the quadratic energy well for rigid particles at a water-oil interface. (C) The adsorption energy ratio of rigid-particle over perfectly-soft-particle. (D) The adsorption energy of soft particles is normalized by the adsorption energy of a rigid particle for various values γ_p/γ_{ow} , where dashed/continuous curves correspond to Poisson ratio $\nu = 0.4/0.5$ respectively. Fig. 4 C and D are from Style et al. [90].

lead to an unfavorable adsorption condition. Despite the negative charges of both silica nanoparticles and glass surfaces, adsorption may still be feasible [97].

The DLVO interaction profile shows that unfavorable adsorption can pertain through a fraction of particles in the secondary energy minimum, some particles with enough energy to overcome the energy barriers to reach the primary minimum, and the intrinsic charge heterogeneity of particles/solid surface providing some favorable site for attachment [93,98]. Meanwhile, salinity and pH can adjust the surface charge and electrostatic interaction between nanoparticles and solid surfaces. For example, both silica nanoparticles and glass or some calcite surfaces will be more negative at higher pH, the electrostatic repulsion between the surfaces becomes more prevalent, and adsorption decreases. In high salinity environments, the electrostatic repulsion vanishes due to compression of the electric double layer, and the pure attractive interaction is achieved [63,73]. Moreover, the competition between flow rate and adsorption force also determines the particle adsorption state [96,99]. For example, at high injection pressures, hydrodynamic stresses cause particles to be continually deposited and distributed throughout the porous medium. By contrast, at low injection pressures, the relative transport behavior is suppressed, causing particles to localize near the inlet of the medium [96].

Nanoparticles can adsorb on the rough glass surface and form many nanostructures, as shown in Fig. 5A. The adsorption of nanoparticles would induce a composite effect including surface roughness change and

chemical property variation. The Wenzel model and the Cassie–Baxter model are two basic models describing the apparent contact angle related to surface roughness and chemical heterogeneity respectively [100,101]. For multiscale surfaces, the wetting states are different at different length scales, which means a universal description of wetting is needed. Sun et al. [102] has proposed a theoretical framework to describe the wetting state based on the concept of ‘deficit curvature’. The underlying origin of the classical wetting models is shown to be rooted within the proposed theoretical framework. Moreover, the adsorption-induced roughness change is quite different from directly roughening the surface. Therefore, the basic models cannot be quantitatively applied to predict the wettability alteration during the adsorption process, while the qualitative change may be consistent.

Comparing apparent contact angle measurement results of the nanoparticle suspension and the surfactant solution on different substrates immersed in decane with the same interfacial tension, we can elucidate that nanoparticles have negligible impact on wettability on polymethylmethacrylate (PMMA) substrate due to no particle adsorption (Fig. 5B), while the contact angle changes on the glass surfaces are more significant, especially on the rough glass substrate. Prior to contact angle measurements, we cleaned the glass by acetone, absolute ethanol and deionized water for ten minutes sequentially, then dried and soaked in decane for 24 hours. The system wettability was characterized by placing a droplet of injection fluid onto the glass substrate submerged in the decane-filled reservoir. The contact angle change vs time was recorded until a steady-state was reached. Based on atomic force microscopy (AFM), we measured the rough topography of the HF-etched glass chip before and after nanoparticle adsorption, as shown in Fig. 5C and D. After nanoparticle adsorption, the roughness factor as the ratio of surface area to the projected area will be changed from 1.02 to 1.21, the roughness maximum will be changed from 8.70 to 72.50 nm, the roughness average will be changed from 1.15 to 5.47 nm, and the root mean square roughness will be change from 1.46 to 6.82 nm. This nanoscale roughness will influence not only the wettability alteration but also the sub-pore scale multiphase flow.

Fig. 5E compares the thick hydrodynamic water film distribution on the smooth convex surface and the hierarchical micro/nanosurface under various capillary pressure, where the hierarchical micro/nanosurface is formed by adding nanoparticle adsorption roughness on the smooth convex structure, as shown in Fig. 5D. The finite-difference numerical solution of the augmented Young-Laplace equation was obtained with successive overrelaxation for the water film configuration. The DLVO interaction forces are presented in Fig. 2A. On smooth micrometric convex surfaces, there exists a thin film only. However, on the hierarchical micro/nanoscale surface, even at a high capillary pressure $P_c=62$ kPa, the connected thick hydrodynamic water film will form from the thin adsorption film and remain robust on the convex surface. This robust thick hydrodynamic film will affect the macroscopic multiphase flow consequences.

2.2.3. Particle ordering kinetics in the thin film

Thin water film widely exists in multiphase displacement processes in porous media, such as the film region between two squeezed oil droplets, the water film region adsorbed on the wall, and the confined three-phase contact region. When the film thickness is ultra-small, the augmented Young-Laplace equation [103] governs interaction with thin water film in the confined three-phase contact region, $P_c = \frac{2\gamma}{R} + \Pi(h)$, where γ is the interfacial tension, R is the curvature radius, Π is the disjoining pressure, and h is the film thickness. Disjoining pressure usually refers to the force that tends to disjoin or separate two interfaces [67]. For simple liquids with no particles, the disjoining pressure dominates when the film thickness is a few nanometers, and it can be calculated by the extended DLVO interactions, which have been introduced in Section 2.2.1.

The spreading coefficient S determined the water spreading behavior

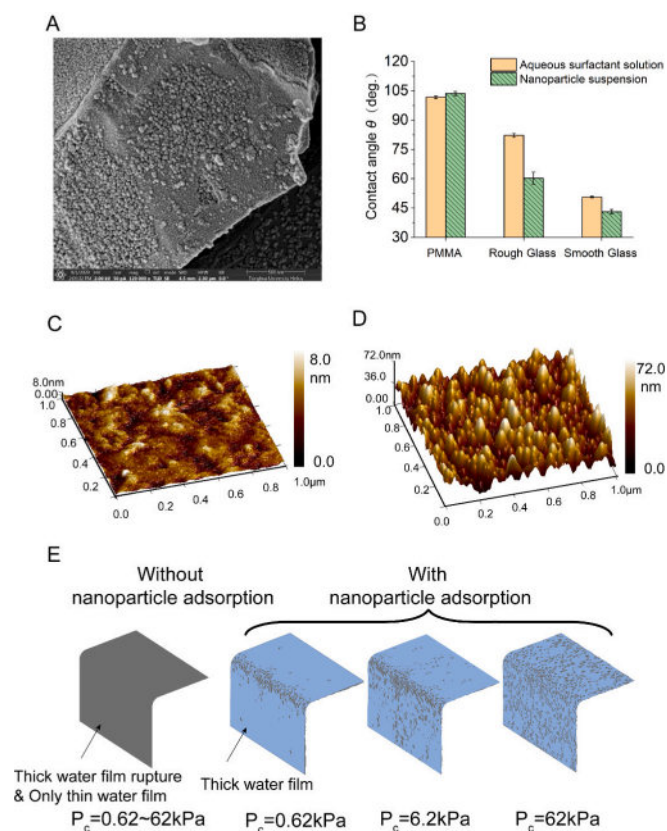


Fig. 5. (A) Nanoparticle adsorption on the rough glass substrate. (B) Comparison of contact angle results of nanoparticle suspension - decane system and surfactant - decane system on the different substrates but with the same interfacial tension. (C) Rough structure characterization of fabrication roughness by HF etching on the glass substrate, and (D) Nanoparticle-adsorption induced roughness on the glass substrate. (E) Calculated aqueous-nonaqueous fluid interface on the hierarchical micro/nanostructures under different capillary pressures; the blue color is the hydrodynamic water film. The curvature radius of the convex surface is about 100 nm, which is much larger than the nano roughness.

which can be calculated by the Frumkin-Derjaguin equation, $S = \Pi(h_e)h_e + \int_{h_e}^{\infty} \Pi(h)dh = \sigma(\cos\theta_e - 1)$, where θ_e is the equilibrium contact angle, h_e is the equilibrium water film at the plain region. The spontaneous film spreading ($S > 0$) of simple liquids only occurs under ultra-wetting state. Based on the Frumkin-Derjaguin equation, the equilibrium contact angle should be zero for spreading. However, a “zero” contact angle does not exist, and spreading occurs in non-equilibrium conditions under realistic situations. The spontaneous spreading of the wetting phase is driven by the force imbalance between the solid/non-wetting phase interfacial tension and the summation of the solid/wetting phase. For nanoparticle suspensions, Wasan and Nikolov [104] found that nanoparticles ordered in the thin film can significantly enhance the film wetting and spreading behavior (Fig. 6A and B). The structural disjoining pressure Π_{str} was proposed to elucidate this unique phenomenon, which has been demonstrated by experimental observations [104], numerical simulations [105], and theoretical derivations [106]. The solid-like particle ordering in the thin-film region increases the system's entropy compared with the greater freedom of nanoparticles in the bulk region. This interesting particle ordering phenomenon results in excess disjoining pressure to enhance the separation of the interfaces and the spreading of the film. It should be noted that the structural disjoining pressure Π_{str} here is induced by nanoparticles ordering in confined film region, which is different from the short-range structural force Π_s introduced in Section 2.2.1. Compared with the traditional disjoining pressure components originates from the extended DLVO forces, this excess pressure a long-range force and dominates when the film thickness is close to the effective particle size.

Extensive efforts have been made to understand the mechanism of particle ordering and structural transitions of suspensions in thin films. Crystallized polystyrene particles confined into a thin film layer have observed that there exists a series of structural transitions as the film thickness changes [107]. Nikolov and Wasan [108] further detected the structural transition of concentrated silica nanoparticle suspensions from periodic colloid structures to local particle networks or clusters due to particle binding or sticking using the reflected light interferometric and the transmitted multiple light scattering imaging techniques. They

presented the phase diagram for the order/disorder structural transition and the film stability as a function of particle concentration, particle diameter, and film thickness. Moreover, simulations of hard spheres in a wedge-shaped cell showed a tendency for the spheres near the vertex to be solid-like or confined and those far from the vertex to be fluid-like or freely moved [105]. These layered ordering structures have been demonstrated by Monte Carlo simulations of hard-sphere-hard-wall and Leonard-Jones systems [109], which become more pronounced as the particle concentration increases. The structural disjoining pressure has been calculated according to the contact between particles and film surfaces, which oscillate with the film's stepwise thinning, as shown in Fig. 6C and D.

The analytical solution of Π_{str} can be derived directly using statistical mechanics based on the hard-sphere model and the Ornstein-Zernike relation [106]. The derivation considers the disjoining pressure between a pair of large spherical particles with radius R immersed in a suspension composed of spherical particles with diameter $d \ll 2R$, which can also be extended to the situation with flat surfaces. The Percus-Yevick (PY) theory [110] is applied to obtain the relation between the macroparticle radial distribution function $g(r, R)$ and the potential of mean force between giants $w(r, R)$, $\frac{w}{kT} = -g + 1$, where r is the distance between the large spheres. The Derjaguin approximation is used to establish the relationship between $w(h + 2R, R)$ and the excess interaction energy per unit area $W(h) = \lim_{R \rightarrow \infty} \frac{-\partial w(h+2R, R)}{\pi R \partial h}$, where h is the distance between two surfaces. By differentiation of the energy to film thickness, we can get the pressure exerted by the hard-sphere fluid film, namely the structural disjoining pressure Π_{str} . In summary, the model related Π_{str} with $g(r, R)$, and the analytical result for the Laplace transform of $g(r, R)$ can be obtained and substituted. Additional corrections should be involved when the film thickness is less or equals one layer of dispersed particles leading to invalid PY theory. The expression of Π_{str} can be calculated by $\Pi_{str}(h) = \begin{cases} -P, & 0 < h < d \\ \Pi_0 \cos(\omega h + \varphi_2) e^{-\kappa h} + \Pi_1 e^{-\delta(h-d)}, & h \geq d \end{cases}$, where $\Pi_0, \omega, \varphi_2, \kappa$ are fitted as cubic polynomials in terms of the particle volume fraction φ , P is the

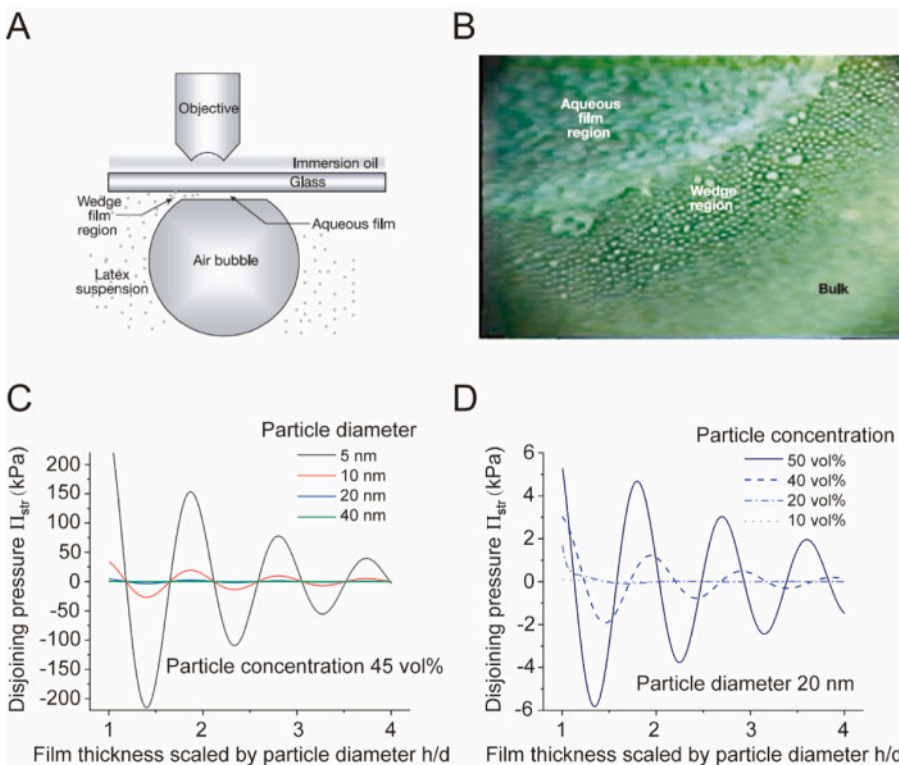


Fig. 6. (A) Diagram of experimental set-up for particle ordering in the confined three-phase region. (B) Particle structuring in a wedge film. Latex particles had a diameter 1 μm , charge 0.8 $\mu\text{C cm}^{-2}$, and occupied 7 vol%. (C) The effect of particle diameter on structural disjoining pressure Π_{str} , where the effective particle concentration is 45 vol%. (D) The effect of particle concentration on structural disjoining pressure Π_{str} , where the effective particle diameter is 20 nm. Fig. 7A and B are from Wasan and Nikolov [104], and data from Fig. 7C and D are calculated based on the theory and method proposed by Trokhymchuk et al. [106].

bulk osmotic pressure of the rigid spherical particle suspension, and $\Pi_1 e^{-\delta(h-d)}$ is a correction term for the film pressure at the separations $d \leq h < 2d$, where Π_1 and δ are determined by the boundary condition of disjoining pressure $\Pi_{str}(h) = -P + \rho kTZ$ at film thickness $h=d$, where ρ is the particle number density, k is Boltzmann number, T is temperature, and $Z = \exp(\beta\Delta\mu)$. $\beta\Delta\mu$ refers to the chemical potential, where $\beta = 1/k_B T$, and $\Delta\mu$ is the configurational chemical potential. $P = \rho k_B T \frac{1+\varphi+\varphi^2-\varphi^3}{(1-\varphi)^3}$ and $\beta\Delta\mu = \varphi \frac{8-9\varphi+3\varphi^2}{(1-\varphi)^3}$ can be derived from the Carnahan-Starling equation, which is an approximate but quite good equation of state for the fluid phase based on the hard-sphere model [111,112]. Fig. 6C and D present the influence of effective particle diameter and particle concentration on the disjoining pressure curve by varying the film thickness, respectively. Smaller effective particle diameter and higher particle concentration contribute to greater disjoining pressure amplitude.

2.2.4. Particle deformation and transport kinetics

A promising approach for improving displacement efficiency relies on the injection of deformable particles into a porous subsurface reservoir [24]. As the deformable particles squeeze through the pore space, they deform, eventually clogging higher permeability regions and diverting flow to harder-to-access pores. This particle deformation and transport kinetics is affected by particle deformability, particle size and pore size ratio, and flow conditions, such as injection flow rate, and point-to-point or piston-type injection methods. In addition, multiple particles may present different behavior compared with isolated particles. For example, multiple particles can unexpectedly squeeze through large-aspect ratio constrictions, which arise from pairwise flow-mediated interactions between the particles due to locally increased hydrodynamic stresses. When one particle is plugged into a pore constriction, the local flow pressure will increase around this particle and enable the subsequent smaller particles to squeeze past. This cooperative mechanism of multiple particles in porous media causes the particles to self-sort based on particle size in the pore space [113]. These processes by which deformable particles squeeze through pore

constrictions, or instead get stuck, critically impact subsequent transport through the entire medium.

2.3. Macroscopic suspension properties

2.3.1. Interfacial tension

The fluid–fluid adsorption kinetic determines the interfacial tension between the suspension fluid and another fluid. By monitoring the decrease in interfacial tension upon particle binding, the adsorption energy of microparticles and nanoparticles at the water–oil interface can be experimentally measured [114,115]. Cryo-SEM has clearly shown that suspended particles can adsorb and densely pack at the oil–water interface [116], as shown in Fig. 7A.

The adsorption kinetics of deformable particles at the fluid–fluid interface can also be evaluated by the dynamic evolution of oil–water interfacial tensions under different conditions, affected by particle concentration (Fig. 7B), temperature (Fig. 7C), and particle deformability (Fig. 7D) [117]. When spontaneous adsorption of particles to the oil–water interface, the interfacial tension will decrease with time increasing. Higher particle concentration, higher temperature, and lower stiffness of particles can promote particle adsorption and stabilize the oi–water interface by reducing the interfacial tension.

The effect of rigid nanoparticle suspension on reducing the interfacial tension by adsorption at the liquid–liquid interface has been widely reported [114,118]. It always presents a similar effect to weak surfactants [119,120]. For example, A 4 wt% silica nanoparticle suspension with a nominal diameter of 20 nm can decrease the interfacial tension of the water–decane system from 48.5 to 44.3 mN/m, while only 0.02 wt% Sulfobetaine 12 surfactant or 0.01 wt% Sodium dodecane sulfonate aqueous solution can achieve a similar effect of interfacial tension reduction from 48.5 to 43.1 mN/m. This interfacial reduction ability can be enhanced when the nonaqueous phase contains active substances such as the complex properties of crude oil. The silica nanoparticle has the more obvious ability to decrease the interfacial tension in the brine–crude oil system from 19.2 to 9.6 mN/m at a concentration of 0.01 wt%, and the interfacial tension is sensitive to nanoparticle concentration

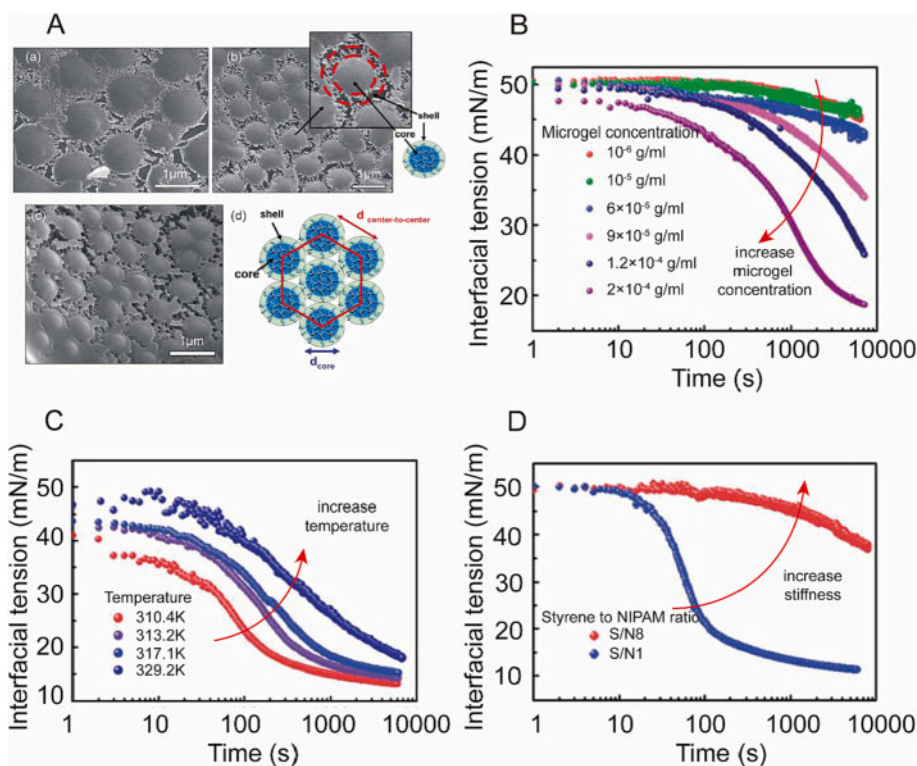


Fig. 7. The relationship between interfacial tension and adsorption kinetics of microgel particles at the fluid–fluid interface. (A) Cryo-SEM image of the heptane–water interface covered by (a) and (b) 2.5 mol% BA crosslinked microgel particles and (c) 5 mol% BA crosslinked microgel particle, the particle structure and arrangement at the interface can be illustrated by (d), where BA is N,N'-Methylenebis (acrylamide), Fig. 7A is from Destribats et al. [116]. (B) Microgel concentration dependence of interfacial tension at the heptane–water interface and 298K, in which the used particles are 3.2% BA PNIPAM microgels. (C) The effect of temperature on interfacial tension at the heptane–water interface, in which the used 3.2%BA PNIPAM microgel concentration is fixed at 5×10^{-3} g mL⁻¹. (D) The effect of stiffness on interfacial tension at the heptane–water interface, in which poly(styrene-co-NIPAM) particles with different styrene to NIPAM ratios to adjust particle deformability, S/N1 can be regarded as a particle with a soft shell, resembling soft microgels, while S/N8 should be regarded as a rigid particle with a very thin layer of dangling PNIPAM chains at the surface. Fig. 7B, C, and D are from Li et al. [117].

[121].

2.3.2. Wettability

Particle adsorption on the fluid–fluid and fluid–solid interface determines the system's wettability. The wettability alteration effect of suspensions can be affected by particle size, cosurfactants, pH value, and ion strength [29,63,122]. The wettability alteration process by nanoparticle suspension is time-dependent that may take days to finish due to the dynamic particle-solid adsorption processes [95,123]. Common wettability alteration explanations are that particle adsorption on the

solid surface alters the surface morphology or suspension contentment impacts the extended DLVO force at the three-phase contact area [124–126]. After adsorption, the classical theories of the Wenzel model or Cassie model are widely accepted to explain the wettability alteration mechanism [127]. The Wenzel model presents that nanoparticle adsorption will increase the roughness factor, the ratio of actual surface area to the geometric surface area, to decrease the aqueous fluid contact angle [128]. The Cassie model presents that nanoparticle adsorption-induced rough structure will contain retained water in the valley of the rough structure, which will increase the nonaqueous fluid contact

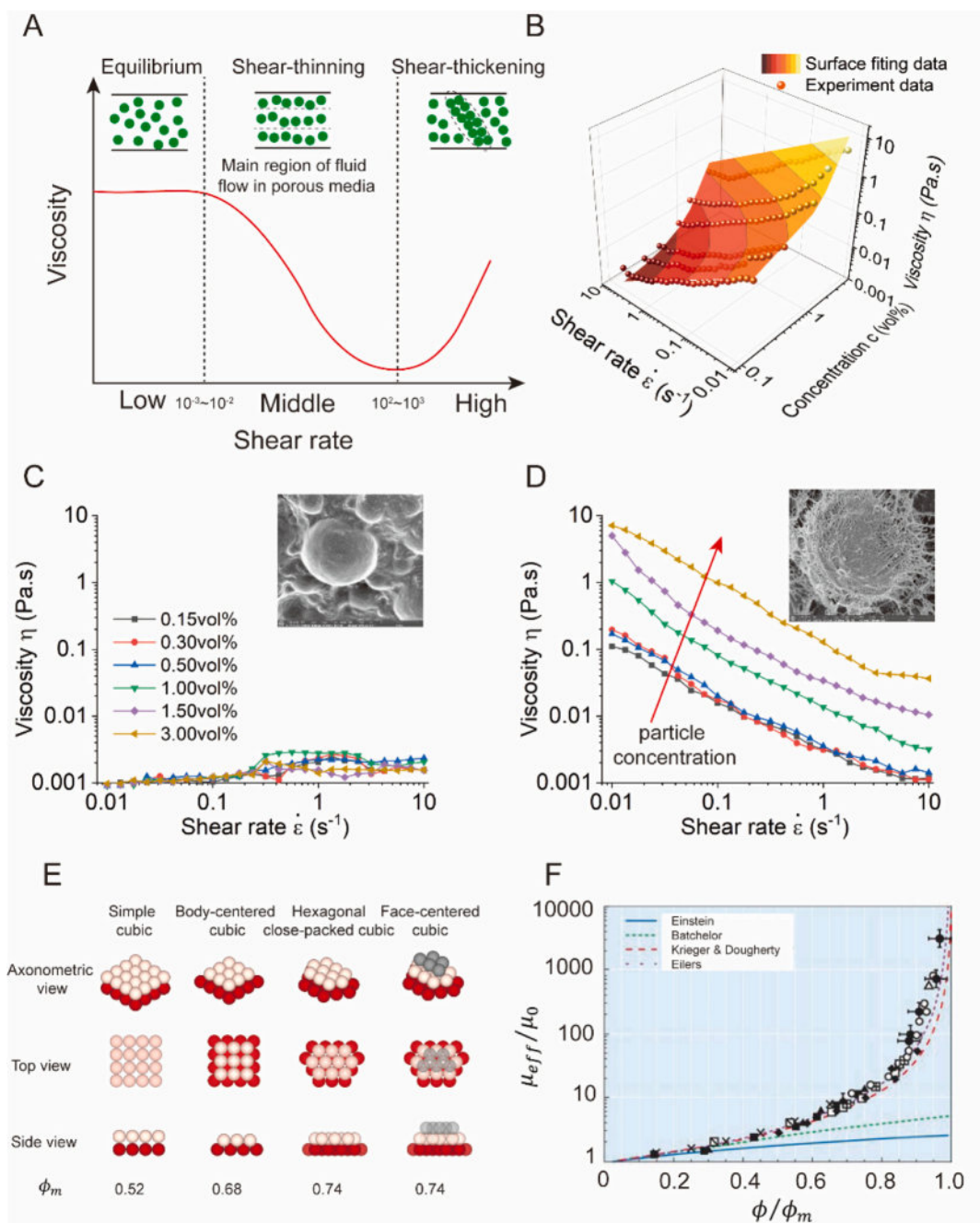


Fig. 8. The typical rheology curve of suspensions and concentration-manipulated rheology of microgel particle suspension. (A) Schematic illustration of three stages in the rheological curvature. (B) The surface fitting of the relation between viscosity, shear rate, and particle concentration. (C) Viscosity curves of different microgel particle concentrations in the oil phase (decane). (D) Viscosity curves of different microgel particle concentrations in the aqueous phase. (E) Sphere stacking schemes with different maximum occupied volume solid fractions. (F) Relative viscosity as a function of reduced volume fraction. The line graphs correspond to models presented by Einstein, Batchelor, Krieger and Dougherty, and Eilers in the text, with $\phi_m = 0.65$ and $[\mu] = 2.5$. The symbol data are from Chang and Powell [143]. The data in Fig. 8C and D are from Lei et al. [36] and Fig. 8F is from Stickel and Powell [147].

angle [100]. Some multiscale rough-patterned surfaces formed by nanoparticle adsorption were also investigated, and the wetting regime on the solid surface can be determined by combining the Wenzel and Cassie–Baxter models [101,129]. The nanoparticle effects on wettability alteration can also be evaluated and analyzed through surface forces and DLVO theory. The fraction of silica nanoparticles covered sites will change the combination of hydrophobic and hydrophilic areas, significantly influencing the structural disjoining pressure or electrokinetic properties and determining the final contact angle data [125,126,130].

2.3.3. Rheology

Deformable particle suspension commonly presents a non-Newtonian behavior, which typically goes through three stages in the rheological curvature [131,132], as shown in Fig. 8A. Deformable particle suspension maintains a constant viscosity at ultra-low shear rates due to repulsive interparticle electrostatic or Brownian forces [133]. With the shear rate increase, the apparent viscosity of deformable particle suspension decreases, classified as shear-thinning properties [134]. The deformable particles move closer to shear orientation layers by the increased hydrodynamic force. However, when the shear rate exceeds a critical value, deformable particle suspension presents shear-thickening properties; the apparent viscosity will increase due to the formation of particle clusters limiting the shear flow [135,136]. During injecting process relevant to the geological system, the shear rate typically ranges from $\approx 10^{-3}$ to 10^3 s^{-1} [137]. Therefore suspensions in these conditions usually present shear-thinning properties. The non-Newtonian characteristics of microgel particle suspensions are controlled by the shear rate $\dot{\epsilon}$ and concentration c , viscosity η follows the fitting relationship $\eta = (10^{0.11c^2+0.62c-2.56})\dot{\epsilon}^{-0.786}$ [36]. Decreasing the shear rate or increasing the particle concentration will increase the apparent viscosity (Fig. 8B). The microgel particle suspension presents the dual characteristics of colloids and polymers with concentration-dependent non-Newtonian characteristics. Well-dispersed microgel particles in stock microgel particle suspension always present Newtonian fluid due to good dispersibility and locked polymer chains inside the particles (Fig. 8C). In contrast, microgel particle suspension in aqueous circumvention presented the shear-thinning features as a power-law fluid at a shear rate range of 10^{-2} to 10 s^{-1} due to the hydrophilic polymer chains on the surface of the particles and the networked structure (Fig. 8D).

Unlike deformable polymer particles with porous structures and polymer chains on the surface, the rheological properties of rigid particles only originate from particle–fluid and particle-to-particle interactions. At low particle concentrations, a flow field around a single sphere can be assumed to describe the increased viscosity, and an increased resulting viscosity is calculated from the viscosity of the solvent and the volume fraction of the dispersed hard spheres, $\mu_{eff} = \mu_0(1 + 2.5\phi)$, where μ_0 is the viscosity of the liquid phase, and ϕ is the solid fraction in the suspension [138]. The formula was modified and adapted for monodisperse suspensions for maximum solid fractions of 0.15 to 0.2 by Batchelor [133] for Brownian suspensions in any flow, $\mu_{eff} = \mu_0(1 + 2.5\phi + 6.2\phi^2)$. One empirical Eilers equation [139] that can overcome the high particle concentration limits was written as $\mu_{eff} = \mu_0(1 + 1/2 [\mu]/\phi/(1 - \phi/\phi_m))^2$. The rheology of rigid nanoparticle suspension is strongly dependent on the solid fraction that effective viscosity increases with the particle volume fraction ϕ , where ϕ_m is the maximum solid fraction in the suspension when the suspension can flow, $[\mu]$ is the intrinsic viscosity as a measure for the particle shape, $[\mu] = 2.5$ for spheres. Suspensions with an even higher solid fraction can also be described with the model of Krieger and Dougherty [140], $\mu_{eff} = \mu_0(1 - \phi/\phi_m)^{-[\mu]\phi_m}$. Assuming spherical particles, the theoretical ϕ_m can be 0.52 to 0.74, depending on the sphere stacking scheme that simple cubic $\phi_m=0.52$, body-centered cubic $\phi_m=0.68$, hexagonal close-packed and face-centered cubic $\phi_m=0.74$, as shown in Fig. 8E. It is also well-

established that for random close packing of spheres the value ϕ_m is about 0.64 [141]. These theoretical analyses of the viscosity versus concentration presented above have been overlaid on experimental data in Fig. 8F.

Smaller particles result in a higher viscosity for a given shear rate and solid fraction. The broader the particle size distribution, the larger the positive effect on the packing density. Polydisperse suspensions usually have a higher maximum packing density ϕ_m as the space can be filled more efficiently compared to monodisperse suspensions. The polydisperse mixture will reach a viscosity minimum when comparing the viscosity of two monodisperse and a polydisperse particle size distribution [142,143].

At low particle concentrations (<5 wt.%), the suspension exhibits a Newtonian behavior, and particles do not significantly impact the aqueous viscosity [144]. However, when nanoparticles were used as foam or emulsion stabilizing agents, some displacement experiments in porous media have shown that these combined nanoparticles systems can substantially lead to higher flow resistance for flow profile control by increasing the apparent viscosity of the displacing phase [145] or nanoparticle-induced fluid–fluid surface hardening [146].

2.3.4. Elastic modulus and strength

The elastic modulus or strength of deformable particles can be evaluated from macroscopic suspension to single microscopic particles. From the suspension view, the strength of suspensions can be characterized by the storage modulus via the rheometer. The storage modulus of suspensions was the ability to store elastic energy that could be recovered eventually. Their values commonly range from 0.1 to 1000 Pa, depending on the material, particle concentration, and particle size [38,40,131,148]. From the particle material view, the elastic modulus and strength of bulk material can be measured directly to represent the values of deformable particles via the uniaxial compressor. The compressive stress–strain curves of different bulk materials of deformable particles show that the compressive strength generally ranges from 0.05 to 10 MPa, and the elastic modulus ranges from 0.1 to 20 MPa [28,149]. From the single-particle view, the elastic modulus of sub-millimeter deformable particles can use regular force-indentation measurements performed by parallel plates in a rheometer. The power-law of particle elastic modulus and particle radius has been obtained [4]. Considering the particle size effect (for micro or nanoparticles), Lei et al. [150] first measured the in situ microscopic elastic modulus of microgel particles in suspension using an Atomic Force Microscope (AFM) to conduct the nanoindentation experiments. They claimed that the in situ elastic moduli of microgel particles with micron diameter in the suspension is about 3.22 MPa, which keeps a relatively larger value. Compared with deformable particles, the elastic modulus of the rigid nanoparticle is order-of-magnitude larger, such as 50–100 GPa for silica-based nanoparticles and 1–50 GPa for polymer-based rigid nanoparticles [151].

3. Microfluidic chips: Fabrication and design

Microfluidics provides the ability to design pore space geometries with different length scales, which can offer an unprecedented visualization resolution in porous media ranging from the interface phenomena at the pore scale to flow patterns at the macroscopic scale [152,153]. Because flow phenomena reside in micro- or nano-structures, microfluidic chips containing flow geometries that match real-world porous media are also called micromodels [15]. Interestingly, micromodel as a microfluidic approach predates the concept of microfluidics, which has been widely used in petroleum engineering, soil/groundwater remediation, and geological carbon dioxide sequestration. In this review, the microfluidic chip and the micromodel have the same meaning and no difference in the concept.

Compared with the multiphase flow in open systems or macro-scale geometries, multiphase flow in porous media is usually characterized by

a relatively low flow rate ($u_p \approx 10^{-2} \sim 10^2 \mu\text{m/s}$) at a low Reynolds number [17] ($Re \equiv \frac{\rho u_p d}{\eta} \approx 10^{-11} \sim 10^{-3}$), and capillarity dominated at a small capillary number [154] ($Ca \equiv \frac{\rho u_p d}{\gamma} \approx 10^{-10} \sim 10^{-3}$), where ρ is the fluid density, u_p is the characteristic flow velocity at the pore scale, d is the characteristic pore size ($d \approx 10^{-1} \sim 10^2 \mu\text{m}$), γ is the displacing fluid viscosity, u_D is the Darcy flow velocity of displacing fluid. Reynolds number Re describes the relative importance of inertial stress to viscous stress, and the interpretation of capillary number Ca is the ratio of pore-scale viscous stress to capillary pressure.

During the last 70 years, microfluidics has gradually developed as a valuable window into the inaccessible and opaque process of complex fluid flow in porous media. Chatenever and Calhoun [155] manufactured one of the earliest micromodels by filling the monolayer glass beads to investigate pore-scale flow mechanisms of the brine displacing crude oil process. Mattax and Kyte [156] first used the term micromodel to describe etched glass-based capillary network models when they observed the waterflooding process under strongly and weakly water-wet conditions. Since then, microfluidics or micromodels have long been applied to study fluid flow in porous media. The selected milestone of micromodel developments is shown in Table 1. Signs of progress have been made in fabrication technology, materials, surface properties, geometrical design, etc.

3.1. Materials and fabrication

The optically accessible porous structure is the basic requirement to visualize the multiphase displacement. The alternative material options for microfluidic chips include glass, silicon, and polymer materials such as polydimethylsiloxane (PDMS) and polymethyl methacrylate (PMMA). Nearly all these materials need to go through at least three steps [177]: 1) transferring the designed pattern on the photoresist-covered substrate by photolithography; 2) shaping the geometrical patterns on the target material, such as dry or wet etching for glass and silicon, replica molding for PDMS, and laser engraving for PMMA; 3) sealing the micromodel against a slide with inlet and outlet ports.

Glass and silicon are the two most common inorganic materials that have been widely used to fabricate microfluidic chips. Since silicon is opaque, the silicon wafer with structure patterns is usually bonded with a glass plate to be observed under a microscope. The wettability of glass or silicon can be easily modified by methods like thermal oxidation [178], salinization reaction [123], and surface coating [32]. There are different kinds of glass or silicon materials, which can also supply many different wettability options; for example, the glass plate of Schott BF33 is more hydrophilic than Schott B270. As for polymer-based micromodels, PDMS and PMMA are the two most extensively used polymer materials, and they are relatively cheaper and easier to fabricate microfluidic devices. Notably, at the molecular level, PDMS is a porous matrix of Si-O backbones covered with alkyl groups, which allows the good permeability of PDMS to oxygen and carbon dioxide. It makes it well suited for cell-culture-involved applications, but also leads to some major problems in certain gas-related displacement. Many nonpolar solvents, such as hydrocarbons, dichloromethane, and toluene, cannot be applied in PDMS microfluidic chips because PDMS swells by adsorbing these solvents. Irreversible decay of the chemical, mechanical, and thermal properties of PDMS also limits their applications in complex circumventions. The chemical resistance and mechanical stiffness of PMMA are more substantial than PDMS but still weaker than glass. The geometrical resolution of the PMMA-based micromodel is relatively lower than other methods. Silica surfaces are usually high charge density, hydrophilic, with extensively studied properties and surface chemistry, while polymer surfaces typically show lower surface charge density and hydrophobicity, and their surface charge often comes from unknown sources or is affected by fabrication techniques [179,180].

To mimic the chemical and physical properties of natural porous

Table 1
Developments of micromodel.

Year	Materials	Model and method	Description	Ref.
1952	Glass bead	The monolayer glass bead packing model	One of the pioneering micromodels	[155]
1961	Glass	Etched micromodel with the capillary network model	The early etched micromodel and the term micromodel proposed for the first time	[156]
1968	Glass	A photosensitive protective layer on the glass	Photolithography was introduced to replace the traditional paraffin coating technology	[157]
1979	Silicon	Wet etching in silicon wafer	One of the early silicon-based micromodels	[158]
1983	Polyacetal resin	Polyacetal resin micromodel with regular network	Pore-scale mechanisms for displacement and imbibition in the pore network model	[159]
1986	Glass	Etching both sides of micromodel to achieve different pore depths	The cover plate was also etched to achieve deep pores and shallow throats	[160]
1988	Polyacetal resin	Polyacetal resin micromodel with random pore width in network	A phase diagram about viscous fingering, capillary fingering, and stable displacement	[161]
1995	Quartz sand	Sand packing model observed by photoluminescent volumetric imaging	Photoluminescent volumetric imaging to visualize 3D porous media	[162]
1996	Glass	Micromodel with hand-drawing fracture-matrix pattern	The early investigation of single-phase flow in fractured porous media	[163]
2006	Silicon	Micromodel with the fracture-matrix pattern from a rock thin section	The early investigation of two-phase flow in fractured porous media	[164]
2011	Silicon	Reservoir-on-a-chip fabricated based on the pore network features of a realistic rock	Reservoir-on-a-chip was pioneering proposed and designed	[165]
2011	Silicon	Dual-permeability silicon-based micromodel	Dual-permeability model for the displacement of liquid CO ₂	[166]
2012	PDMS	Dual-permeability PDMS-based micromodel	Dual-permeability model for the displacement of foam	[167]
2012	Glass	Deep reactive ion etched (DRIE) glass micromodel	A dry etching technique was used on a glass micromodel for a large aspect ratio	[168]
2013	Glass bead	Glass beads filled capillaries and observed by confocal microscopy	Confocal microscopy to directly visualize the fluid flow in a 3D micromodel	[169]
2014	Calcite crystal	A real-rock micromodel through etching on calcite crystal	A calcite crystal was etched to maintain the original substrate chemistry	[170]
2016	Photocurable polymer (NOA81)	Micromodels with a wide contact angle (7°~150°)	The systematic study of the wettability effect on the displacement pattern	[171]
2017	Glass	Glass micromodels modified by in situ	CaCO ₃ -coated micromodels could	[172]

(continued on next page)

Table 1 (continued)

Year	Materials	Model and method	Description	Ref.
2017	Glass	growing a thin layer of CaCO ₃ nanocrystals	mimic real carbonate reservoir properties	[173]
		Glass micromodels with varying depth based on one-time etching	Depth variations were introduced based on the traditional fabrication method	
2017	Silicon	A dual-porosity and dual-depth silicon-based micromodel	photolithography to improve the structural realism by dual-depth	[174]
2019	Glass	Glass microfluidics with pore-scale surface roughness	Glass microfluidic chips with controllable surface roughness	[175]
2020	Silicon	Reservoir-on-a-chip designed based on statistical information from real rock	Micromodel owns the most important statistical features of natural rock directly	[176]

media, geomaterial microfluidic chips have also developed and received attention recently. The original surface chemistry largely affects the particle and fluid behaviors in the applications [181]. Direct etching pore structures on the natural crystal is beneficial for observing the preferential dissolution process induced by flow field and crystallographic orientation [170]. More surface structure information can also be reflected to consider their effect on displacement. For example, joint-fracture microfluidic channels designed on natural coal samples

demonstrate that fracture roughness in these systems led to higher pressure differences than traditional PDMS chips [182]. To consider 3D geometrical features, randomly packing particles between transparent parallel plates as one of the earliest micromodels [183–185] or advanced 3D printed models [186–188] also occupies an important position in studying displacement mechanisms. Based on the advanced imaging and reconstruction methods, such as confocal microscope imaging [184,185], X-ray computed tomography [189,190], and photoluminescent volumetric imaging [162], it can be extended to three dimensions to realize the truly 3D geometrical features of the natural porous media. However, the above methods are inevitably limited by the structural accuracy, the structural repeatability, the selection of multiphase fluids, and the synchronous imaging of the full flow field during the displacement process.

3.2. Geometrical designs

The porous structure design is the core part of the microfluidic experiment. Geometrical designs of varying complexity can either simplify unique pore structures or closely mimic the complex geometry of natural porous media, which depends on the corresponding research purposes. Fig. 9 shows several typical microfluidic geometrical patterns ranging from complex reservoir-on-a-chip to purified single pore.

On the one hand, many studies have been devoted to realizing the similarity of some flow characteristics of microfluidic chips and real-world porous media. Different from the traditional geometry extracted from the rock slice image [191] or randomly distributed array structure [171], Kumar Gunda et al. [165] first transferred the statistic network information of natural rock to the microfluidic structure design using stochastic random network generators and Delaunay triangulation, and they proposed reservoir-on-a-chip conceptually. Later, a modified pore network structure was obtained based on a particle density map by

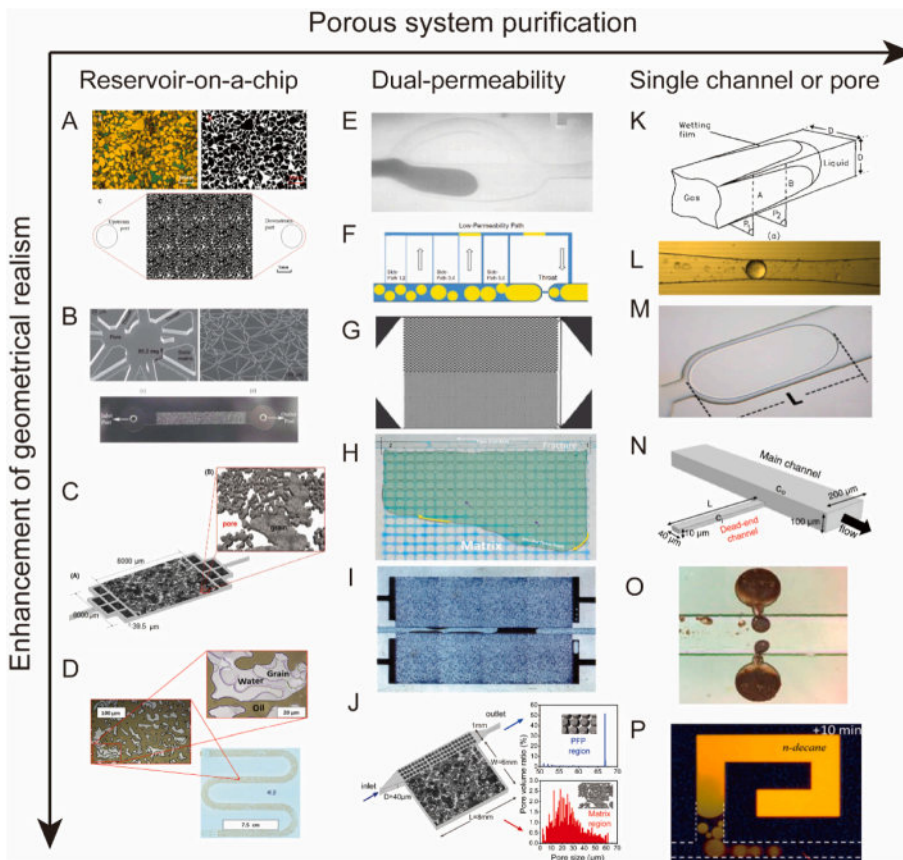


Fig. 9. Various patterns of 2D porous structures contain different statistical features. A. pore structure extracted directly from the rock slice [191]; B. pore-network structure extracted based on the rock pore-network information [165]; C. porous structure regenerated based on real rock statistical information [176]; D. the length of the porous structure equals to the real rock sample [193]; E. parallel two-channel models with different widths [194]; F. parallel two-widths microchannels with several vertical connected channels [195]; G. parallel regular array structure with different permeability [166]; H. regular array structure with bypassed fracture channel [197]; I. hand-drawing fracture-matrix structure [163]; J. the heterogeneous porous media containing preferential flow pathway and parallel matrix region [199]; K. square glass channel [200]; L. constriction channel [203]; M. single pore-throat structure [208]; N. straight dead-end channel [206]; O. dead-end pore [119]; P. non-straight dead-end channel [205].

superimposing CT scan images and dividing pore lines via a watershed algorithm [192]. To make the designed reservoir-on-a-chip similar to the natural rock statistically, Lei et al. [176] regenerated similar 2D structures on the chip by QSGS (quartet structure generation set) to maintain the same pore size distribution and pore structure features of natural rock obtained by micro-CT scanning. Later, more structure features such as the core length [193], locally constricted 3D throat [173], surface roughness [175], and dual-depth of pore and throat [174] were also considered and imported into the reservoir-on-a-chip to enhance the structural realism.

On the other hand, the dual-permeability model or pore doublets as the ideal model was used to purify the flow process in heterogeneous porous media. Chatzis and Dullien [194] conducted the pioneer dual-channel microfluidic experiments and claimed the two classical pore-scale multiphase flow modes of bypass and snap-off. The heterogeneous microfluidic model, including the multiple parallel microchannels [195], the dual-permeability model with vertical posts arrangements [36,166,167,196], and the fracture-matrix model [163,164,197,198], were used to explore the preferential flow suppression effect of the dispersed phase, such as emulsion, foam, and suspension. Recently, the multiphase flow feature of flow heterogeneity was considered in the heterogeneous microfluidic chips, Lei et al. [199] designed a porous microstructure actively containing a high-permeability layer to generate a preferential flow pathway on the microfluidic chip. As a promising bottom-to-top approach, single-channel [200–202], constriction microchannel [146,203,204], and dead-end structures [119,205–207] are designed as fundamental units of porous media to explore the more detailed interfacial phenomena. Higher imaging resolution at the single pore scale enables observation of particle and multiphase transport and interfacial phenomena.

4. Suspension-related displacement mechanism in porous media

Suspension flow dynamics and corresponding multiphase response are fundamental to understanding and optimizing the displacement performance. Recovering or trapping nonaqueous fluid from porous media are major goals of suspension-related displacement in enhanced oil recovery and groundwater remediation. In these cases, characteristic flow velocities typically range between ≈ 0.01 and $100 \mu\text{m}\cdot\text{s}^{-1}$, and the typical pore size range between ≈ 0.1 and $100 \mu\text{m}$. Oil ganglia or the nonaqueous contaminant are trapped in the pores by capillarity or flow heterogeneity. The criterion to displace trapped nonaqueous fluid originates from the balance of suspension sweeping and carrying ability [199]. A more hydrophilic condition, a higher viscosity, or plugging induced flow resistance increasing leads to a stronger sweeping ability, while the carrying ability is determined by the competition between the viscous pressure drop $|\Delta P_v| = \eta(Q/A)L_g/K$ and the capillary resistance induced by the fluid–fluid interface through the pores $|\Delta P_c| \approx \gamma/d$, where η is the displacing fluid viscosity, Q is the flow rate, A is the cross-sectional area, L_g is the ganglia length, K is the permeability, γ is the fluid–fluid interfacial tension, and d is the characteristic pore size [184,185]. Therefore, the effect of suspension on the interface and flow behavior will decide the sweeping area in overall porous media and both the resistance and pressure drop values in the local area. Microfluidic experiments provide a straightforward way to probe the effect of suspension on multiphase displacement in porous media. Such platforms enable the systematic study of the suspension flow dynamics, the flow field evolution, and flow patterns. This section will summarize and discuss the displacement mechanism of rigid nanoparticles and deformable particle suspension by microfluidic experiments.

4.1. Deformable particle suspension

Preferential flow resulting in the non-uniform flow pattern in porous media is one of the most unwelcome phenomena in most displacement processes. Compared with continuous fluid, such as polymer solution,

deformable particle suspension as the typical dispersed system in porous media can present stronger self-adaptivity to the variations of pressure and flow resistance, thus automatically controlling the flow behavior for the uniform flow pattern [176,209]. The excellent capability of deformable particle suspensions has been claimed and demonstrated to have advantages in suppressing the preferential flow through particle plugging and diverting effect, particle concentration-manipulated rheology, and particle adsorption-induced wettability alteration.

4.1.1. Particle plugging and diverting effect

One of the high-performance displacement mechanisms of deformable particle suspension is ascribed to the plugging and diverting effect. Different microfluidic experiments, such as the narrow capillary channel [203,210], artificial network geometry on glass micromodel [131,211], and sand-packing model [212] have been designed and applied to evaluate the transport and retention of deformable particles in the porous structure. Based on these visualization results, the transport modes of deformable microgel particles can be classified as adsorption, direct pass, deform and pass, trapping, and adsorption, where trapping can be further divided into the single particle-plugging mode and multiparticle bridge-plugging mode [211,212] (Fig. 10). The transport and retention modes in the microchannel are mainly controlled by the flow rate, particle elastic modulus, and size matching ratio [203]. For example, small particles with a high flow rate will pass directly, while a low flow rate will result in particle adsorbing on the channel surface [96,213]. The larger elastic modulus or larger particle size may induce a larger friction force due to particle deformation, leading to particle trapping in the porous structure [214].

It is worth noting that nondeformable natural fine material sometimes can also present diverting effects, especially combined with low-salinity flooding. However, these nondeformable microparticles are rarely selected actively as flooding agents in porous media due to harmful plugging in the reservoir. Even for the deformable particles, the reservoir damage formed by particle plugging may also not be ignored when particle size is relatively larger. The selection of suspension agents is usually dealt with as companions during displacement for the balance of plugging and diverting.

During the single-particle deforming and passing process, the deformable particle gets trapped when the pressure difference across the channel is lower than the threshold value. Theoretically, the transport consequences are related to the elastic and shear modulus of the deformation particle and particle-pore size ratio [215]. Based on assuming the deformation of the particle as linearly elastic, this threshold pressure difference can be estimated by balancing the deformation energy with the pressure work, $\Delta P_t \propto E(D_0/d_c)^{4.7}$, where E is the elastic modulus of the particle, D_0 is the original particle diameter, d_c is the diameter of the channel [56] (Fig. 11A). Lei et al. [150] performed an Immersed Boundary-Lattice Boltzmann simulation of a deformable particle with different elastic modulus passing through various throat channels and got the similar threshold pressure difference trend $\Delta P_t \propto E^{1.2}(D_0/d_c)^{5.2}$ (Fig. 11B). Both microfluidic experiments and pore-scale simulations have demonstrated that the critical pressure difference of the linearly elastic particle transporting through an ideal pore-throat channel can be described well by elastic modulus and particle-pore size ratio. The quantitative difference may originate from the elastic modulus characterization, the geometric confinements that microfluidic experiments containing uniform depth but 2D IB-LBM containing infinite depth, and the setting condition difference between numerical simulation and experiments in geometric structures, particle size, injection methods, etc. When the narrow throat channel is a relatively long and deformable particle is confined in the throat totally, the velocity of the particle is approximately constant with a rough balance between the pressure driving force and the resistance, where the friction and adhesion properties between the particle and channel wall should also be considered [214].

Deforming and passing a narrow channel can also occur when the

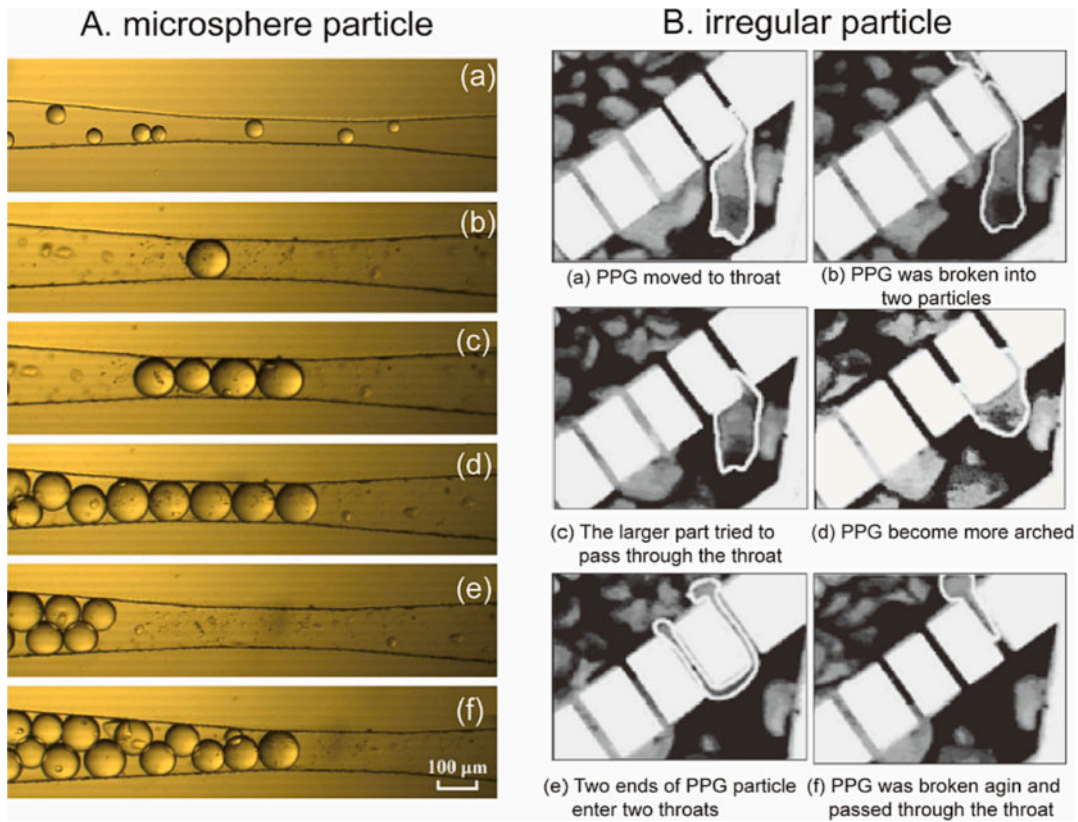


Fig. 10. (A) Microscopic images of polyacrylamide microspheres transport in the microchannel, from absorption and single-particle blocking modes to multiparticle bridging blocking modes. The figure is from Yao et al. [203]. (B) the transport modes of irregular PPG particles through throats at the network micromodel, from direct passing to different blocking modes. The figure is from Bai et al. [211].

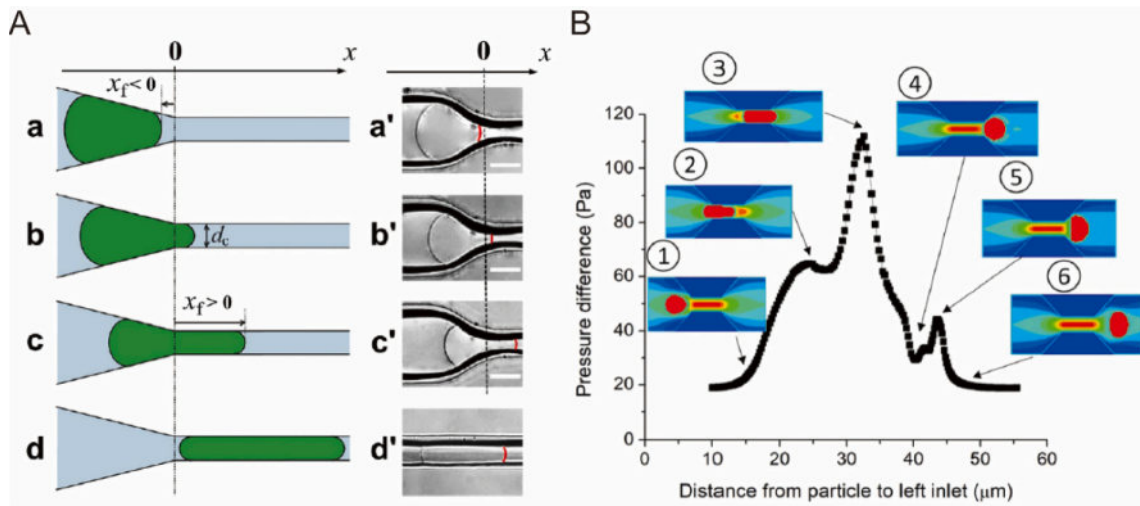


Fig. 11. Microgel particles are forced through a narrow microchannel in different confined states. (A) Schematics and corresponding representative optical microscopy images of the microgel particle in the confined states. Fig. 11A is from Li et al. [56] (B) Simulation results of pressure difference versus particle position variation during the particle transport. Fig. 11B is from Lei et al. [150].

diameter of particles is smaller than the pore size. Several proposed mechanisms rely on the particle bridging effect with the formation of an arch structure of particles across the cross-section of the channel. The probability of arch structure formation increases with the flow rate, the particle concentration, and the ratio of the particle to the pore size [216]. The bridge-like structures are composed of a few particles, typically between 2 and 10 [217]. A bridge structure will form when the particle arrives simultaneously at the channel, and their number is

larger than a critical number, $n_{max} \propto 3A/D_0^2$, where A is the area of the channel cross-section, the accurate critical number can be experimentally determined [218]. The plugging time as the time interval between two arches formation is predicted at a range $\frac{([n_{max}/2]+1)!}{(n_{max}\phi)^{[n_{max}/2]+1}} \frac{AD_0}{2Q} \leq t_{plug} \leq \frac{([n_{max}]+1)!}{(n_{max}\phi)^{[n_{max}]+1}} \frac{AD_0}{2Q}$, where $[n_{max}]$, $[n_{max}/2]$ are the floor of n_{max} , $n_{max}/2$ respectively, i.e., the largest integer that is less than the number, Q is the flow rate through the unobstructed constriction

[218,219]. This model is based on the assumption that the particles are initially uniformly distributed in the suspension, and particles arrive almost simultaneously at the throat of the channel. Microfluidic experiments have been conducted to observe these bridging processes and their results are in good agreement with the theoretical model [218]. The porous media's bridging processes are more complex due to the filter and shunt effect. With a microfluidic chip with a leaky channel flanked by the array posts, the particle blockage pattern can move at a steady speed, and the blockage shape can be controlled by the ratio of the resistance porous wall and the channel [220].

The importance of the size matching rule between the particles and pore throats in porous media for effectively blocking high-permeability pathways and diverting the displacing fluid into low-permeability layers has been figured out [24,26,221]. When suspended particles are injected into porous media, the size matching ratio is defined as the mean hydraulic diameter ratio of suspended particles and pores in the porous media. When the single-particle transport in a single pore-throat channel, it is defined as the hydraulic diameter ratio of the particle and the throat. Unfortunately, inconsistencies in the literature make it difficult to determine the optimal conditions for improved fluid displacement. The optimal size matching ratio varies widely in the different studies, as shown in Fig. 12. On the one hand, the particle size and pore size are usually characterized by the average particle diameter of the suspension and the average pore diameter of the porous medium. However, many microfluidic experiments have found that the transport of suspended particles with different sizes in the porous medium has a cooperative size sorting effect, resulting in different plugging extents [113]. The complex flow field in the porous structure also has a hydrodynamic filtration for continuous concentration and classification of micron particles [222]. Thus, different experiments may get inconsistent results due to various particle and flow dynamics impacting on plugging effect. On the other hand, the plugging effect may not be the only mechanism for improving displacement. Suspensions have been applied for different reservoir conditions ranging from ultra-high to ultra-low permeability layers and achieved variable success [26]. In particular, particles with a

small matching coefficient to freely move through porous media were also reported to effectively reduce permeability and improve immiscible fluid mobilization [223,224]. For example, 3D microfluidic experiments using confocal microscopy demonstrated that small particles with a dilute ($<10^{-2}$ vol%) can increase the viscous stresses on trapped droplets through deposition, thus be harnessed to mobilize and remove trapped fluids from a porous medium up to an additional $\sim 70\%$ [224].

4.1.2. Particle concentration manipulated rheology for self-adaptive effect

Deformable particle suspension commonly contains polymer/colloid duality that the coupling of fluid non-Newtonian features and particle advection-diffusion properties will impact the multiphase flow pattern. Concentration-manipulated rheology may explain why the ultra-small size matching ratio still contributes to the effective displacement. The nonlinear dynamics of miscible flow displacements by coupling the flow field and advection-diffusion processes have been studied in various conditions, such as Newtonian or non-Newtonian fluids [232,233], homogeneous or heterogeneous media [234], and concentration-dependent diffusion coefficients [235]. This nonlinear dynamics of miscible flow displacements is harmful to the realization of the uniform flow in the homogeneous porous media due to instability-induced fingering phenomena. However, during immiscible multiphase displacement in heterogeneous porous media, this fluid flow-particle diffusion coupling effect has been demonstrated to suppress preferential flow effectively and eventually achieve the best displacement in some conditions [36].

At the ideal dual-permeability microfluidic experiments, different multiphase flow patterns displaced by suspensions with different bulk particle concentrations were observed, as shown in Fig. 13A. Three different suspension transport modes were identified: channeling mode at a low particle concentration, synchronous mode at an intermediate particle concentration, and fluctuation mode at a high particle concentration. At an intermediate particle concentration, the synchronous mode can always maintain the lowest invading phase saturation difference and achieve a uniform flow (Fig. 13B). Here, deformable particle

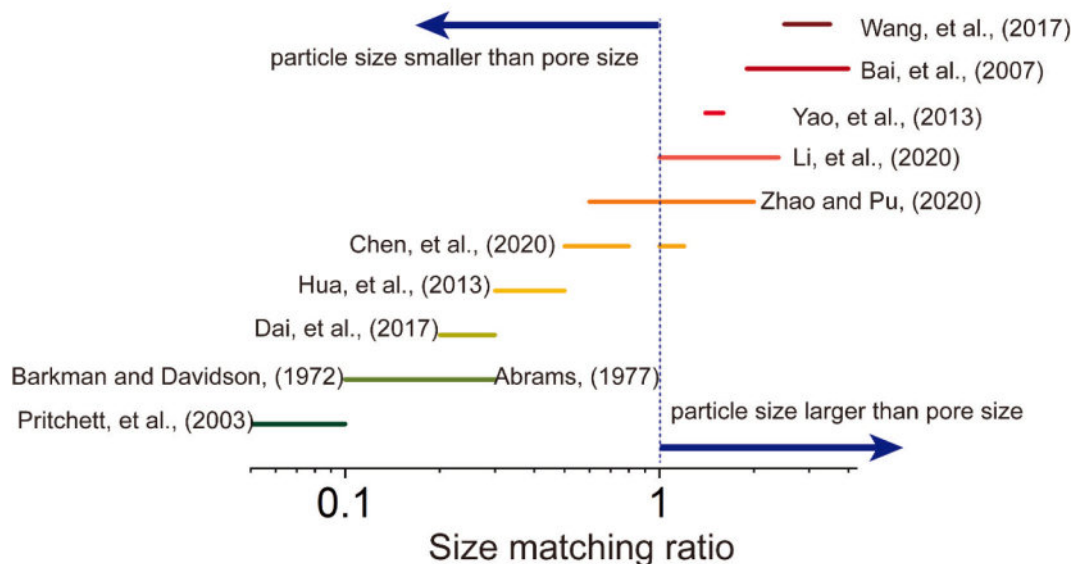


Fig. 12. Literature review about optimal size matching ratio. Size matching ratio < 0.1 , data is from Pritchett et al. [225]; Size matching ratio = 0.14~0.33, data is from Barkman and Davidson [226], Abrams [227]; Size matching ratio = 0.21~0.29, data is from Dai et al. [228]; Size matching ratio = 0.33~0.5, Data is from Hua et al. [27]; Size matching ratio = 0.5~0.8 and 1.0~1.2, data is from Chen et al. [229]; Size matching ratio = 0.59~1.99, data is from Zhao and Pu [230]; Size matching ratio = 1.0~2.4, data is from Li et al. [231]; Size matching ratio = 1.35~1.55, data is from Yao et al. [39]; Size matching ratio = 2.0~4.0, data is from Bai et al. [211]; Size matching ratio = 2.5~3.5, data is from Wang et al. [210].

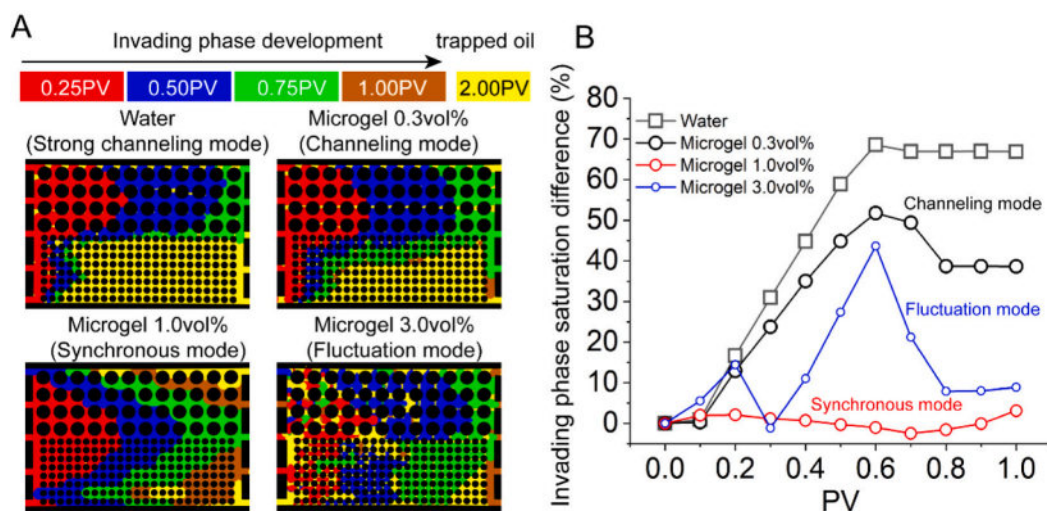


Fig. 13. Microfluidic experimental results of water flooding and microgel particle suspension flooding with different particle concentrations. (A) Multiphase distribution during the displacements of water and microgel particle suspension at different representative stages of 0.25 PV, 0.50 PV, 0.75 PV, and 1.00 PV, PV is the pore volume. (B) the variation of invading phase saturation difference. The characteristic particle sizes (D_{50} , the particle size of the 50% cumulative probability) diluted in the aqueous phase were 2.13, 3.12, and 4.58 μm . The smallest pore size of the microfluidic chip was ten times larger than the particle size, where the throat widths are 60 and 120 μm in higher and lower permeable layers, and the depth of the microfluidic chip is 60 μm . The permeability ratio was estimated at 16:9 with the hydraulic radii of the pore throats. Figures are from Lei et al. [36].

suspension presents concentration-manipulated rheology, $\eta = \left(10^{0.11c^2+0.62c-2.56}\right)\varepsilon^{-0.786}$ [36], which has been introduced in Fig. 8 and Section 2.3.3, the coupling effect of particle diffusion and the effect of non-Newtonian fluids may play a key role in controlling multiphase flow patterns. The porous structure, multiphase fluid properties, and injection conditions in the simulations are the same as those in the corresponding microfluidic experiments. The injection flow rate was set as $Q = 1 \mu\text{L}/\text{min}$. Due to the separation and hydrodynamic filtration caused by particle transport in the long injection tube (observed based on microfluidic experiments), 0.08 PV ($t = 10 \text{ s}$) water was injected first as a buffer layer, and then the injection of microgel particles was started in the simulation.

The corresponding particle concentration distribution in higher and lower permeability layers presents the particle concentration self-adaptive feature, as shown in Fig. 14. The particle concentration in the higher permeability layer was significantly higher than that in the lower permeability layer. However, at a high particle concentration, the hysteresis of the particles will cause a drastic particle concentration increase [236,237]. Thus, the particle concentration and preferential flow frequently change between the higher and lower permeability layers at a high particle concentration. These transport modes were also demonstrated by a pore-scale numerical simulation coupled with non-Newtonian Navier-Stokes equations, an advection-diffusion equation, and the Cahn-Hilliard equation (Fig. 14D). Here, the Cahn-Hilliard equation is the governing equation of the phase-field method, which stands out in its treatment of the interface as a physically diffuse thin layer by spreading the interfacial force over a volume, the detailed calculation can be referred to Lei et al. [36]. As described in Section 2.3.3, the in situ morphology of the deformable particles in the suspension is responsible for the suspension rheology, which is a prerequisite for self-adaptive particle concentration controlling the flow field. The microgel particles present the dual characteristics of colloids and polymers with concentration-dependent non-Newtonian characteristics due to the hydrophilic polymer chains on the surface of the particles and the networked structure, which contributes to the different transport modes in the dual-permeability microchips.

For the more general case in complex porous media, reservoir-on-a-chip experiments also found that deformable particle suspension has a strong self-adaptation of flow field due to the particle diffusion effect and

suspension non-Newtonian effect. Microgel particle suspension with concentration-manipulated rheology presents a novel preferential flow suppression effect in the heterogeneous porous media even when the particle size is much smaller than the pore size. Compared to the continuous polymer solution with similar macroscopic rheology, these microgel particles can achieve a higher displacement efficiency by self-adjusting the flow resistance in the porous media [176,209].

4.1.3. Particle adsorption induced wettability alteration effect

Several proposed mechanisms rely on the potential influence of deformable particles adsorbed on the fluid–fluid and fluid–solid interface. The adsorption of deformable particles could stabilize the fluid–fluid interface because they stretch at the interface and decrease the interface tension [89,238]. Both water–solid and water–oil interface energy will decrease due to the adsorption of particles, while nonaqueous fluid/solid interface energy remains unchanged. Confocal laser scanning microscopy provides a powerful tool to observe deformable particle distribution in the contact area of oil/water/solid systems and the corresponding wettability alteration [239]. The aqueous fluid contact angle will decrease in the microgel suspension with different bulk concentrations. This incremental hydrophilicity may be favorable for improving displacement efficiency, especially alternated from oil-wet to water-wet conditions.

Two main mechanisms have been proposed to connect the deformable particle adsorption and wettability alteration phenomena: the classical tangential force imbalance theory and the disjoining pressure imbalance [104,239]. In hydrophobic conditions, the classical tangential force imbalance is the main factor responsible for the changes in microgel-induced wettability. The microgel particles can be adhesive to the hydrophobic interface and settle irreversibly after adsorption. The adsorbed microgel particles reduced the oil-water interfacial tension and caused the shrinkage of the three-phase contact line. Thus new microgel strips will be formed in this newly exposed contact area. The adsorbed microgels in this new region came from the bulk through diffusion, and the adjacent microgels remained in their original sites regardless of the newly formed microgel strips. Microgel strips result from the contact line retraction process. First, the retraction of the three-phase contact line will supply the vacancies, as shown in Fig. 15. Then the microgel approached the vacancy and finally settled down. The microgels could hardly be detached due to continuously retracting the three-phase

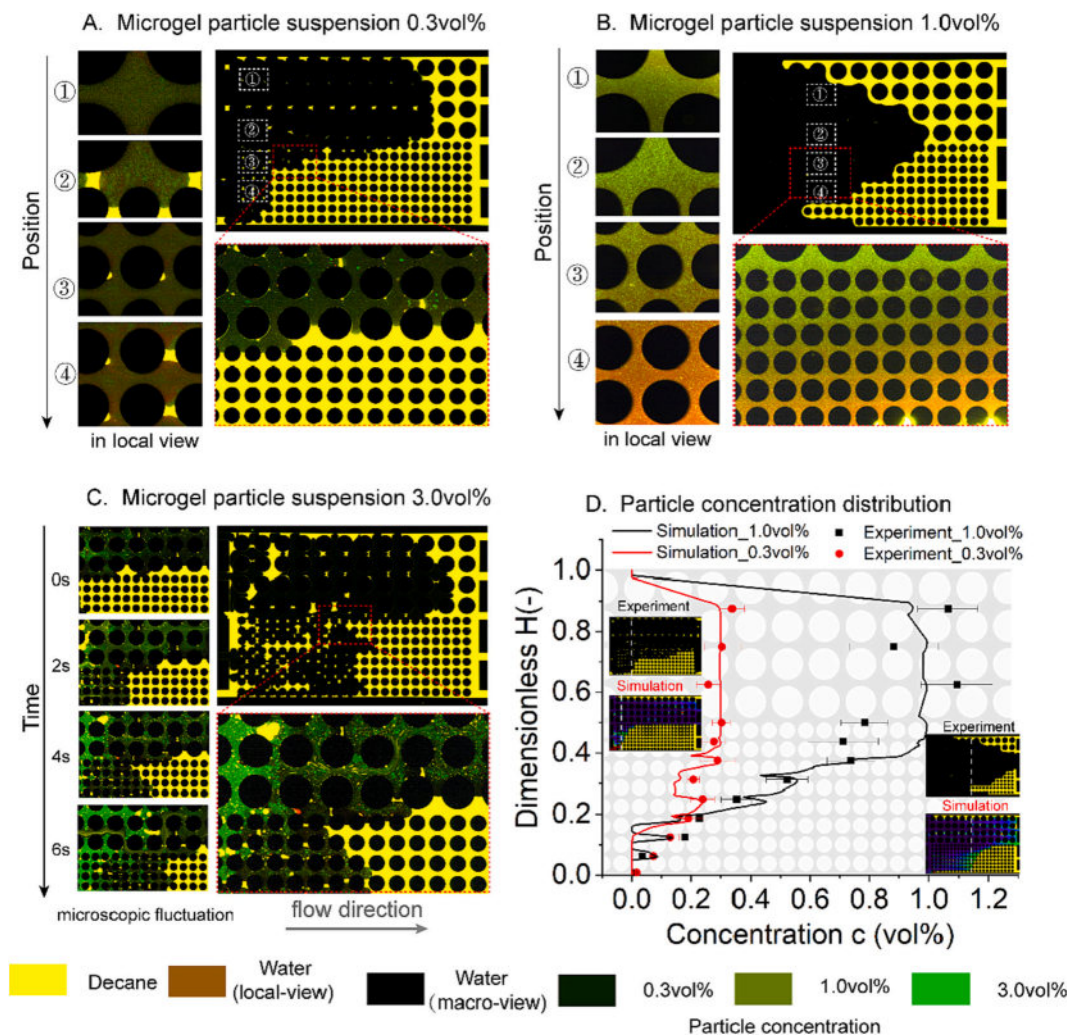


Fig. 14. Microgel particle concentration distribution in the dual-permeability model. (A) Microgel particle suspension flooding with bulk concentration 0.3 vol.%. (B) Microgel particle suspension flooding with bulk concentration 1.0 vol.%. (C) Microgel particle suspension flooding with bulk concentration 3.0 vol.%. (D) Experimental and simulation results of microgel particle concentration distribution at high and low permeability layers with bulk concentrations 0.3 vol.% and 1.0 vol.%. Figures are from Lei et al. [36].

contact line after reaching the vacancy. In hydrophilic conditions, the deposited microgels can assemble into wedge-shaped films and diffuse further to generate structural disjoining pressure, which is one of the most important effects of nanoparticle suspension, and it will be introduced in detail in Section 4.2.3.

4.1.4. Discussion

The aforementioned mechanisms of deformable particle suspension affecting the multiphase flow pattern may significantly determine the multiphase displacement processes. However, the suspension state and application environments in natural and engineering are generally more complex, which challenges the validity of the above mechanisms.

For the suspension state, the above suspensions are considered as the unimodal normal distribution of deformable particles in the suspension. However, the aggregation or dispersion state of the particles in the suspension also affects their transport behavior. Microgel-in-oils [37], as many particles trapped in oil droplets, can also play an important role in improving the displacement performance, especially in the heterogeneous porous structure and after a long displacement time. Comparing the suspensions with different particle concentrations and microgel-in-oil content, microfluidic experiments on the heterogeneous reservoir-on-a-chip with a preferential flow pathway demonstrated that suspension with moderate microgel-in-oil at intermediate particle

concentration yielded the optimal displacement efficiency, microscopic observations in the preferential flow pathway region elucidate that the synergistic transport of microgel-in-oil and microgel particles resulting in local pressure fluctuations and diverting fluid from the preferential flow pathway to the matrix region is responsible to this high-performance displacement behavior, as shown in Fig. 16.

For particle state in the suspension, some deformable particles may swell to several tens or hundreds of times their original particle size in the aqueous phase after several days or months [131,148]. The swelling ratio of the deformable particles is generally influenced by salinity and temperature. Unlike the freedom expansion in suspensions, the extent of deformable particle swelling in the porous structure is determined by the competition between the osmotic force exerted by particle swelling and the confining force transmitted by the surrounding porous structure [4]. The particle's swollen state will influence the elastic modulus of deformable particles, $E \propto (c_p V_0/V)^{2.9}$ where c_p is the polymer concentration during the initial drop formation stage, V_0 is the volume of the drops, and V is the volume of the particles after swelling in water [215], which will influence the plugging and diverting effect. Meanwhile, as for nanoscale deformable particles, the interfacial phenomena will be weakened for larger particles with a smaller surface-to-volume ratio.

For application environments, multiple factors may be coupled and become more complex than the single mechanism mentioned above. For

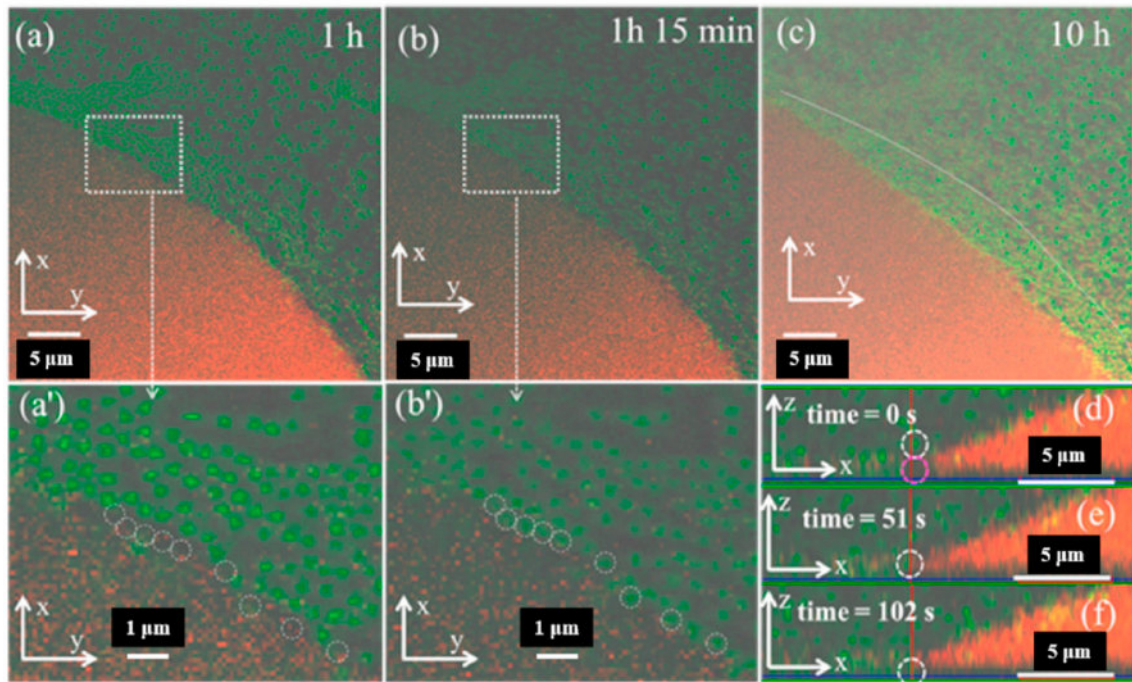


Fig. 15. The evolution of deposited microgels in the three-phase contact line region on the substrate plane at 1 h (a), 1 h 15 min (b), and 10 h (c). the deposition process of the microgel on the selected vacancy was captured at 0 s (d), 51 s (e), and 102 s (f) on the vertical plane of the substrate. Fig. 15 is from Gong et al. [239].

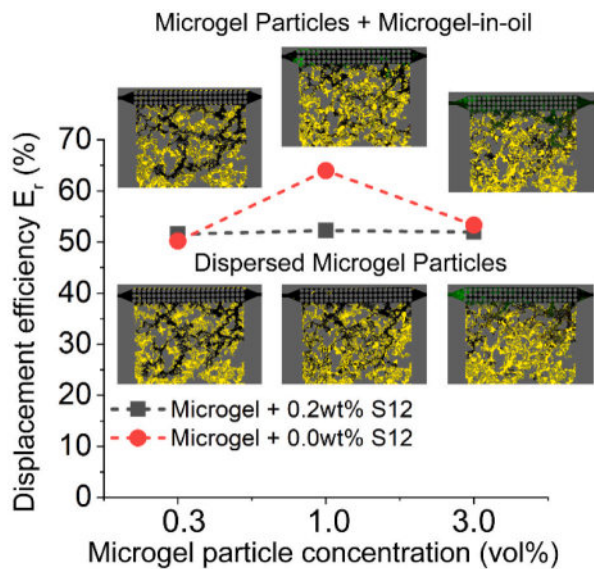


Fig. 16. The influence of microgel-in-oil on displacement efficiency of suspensions with different particle concentrations. Fig. 16 is from Lei et al. [37].

example, cosurfactants are indispensable in formulating deformable particle suspension, significantly impacting interfacial tension, wettability, and particle behaviors. The influence of cosurfactants cannot be ignored in many cases relevant to the mechanism of wettability alteration or interfacial tension reduction. Some glass-etched micromodel experiments [240,241] have observed the synergistic effect of particles and cosurfactant during the displacement in heterogeneous porous media that the residual oil in the high permeability channel is efficiently displaced owing to the interfacial tension reduction, the wettability alteration, and emulsification, meanwhile, the plugging of the particles can divert more water into the unswept low permeability zone.

4.2. Rigid nanoparticle suspension

Extensive industrial applications [121,195,242,243] show that it is still effective for enhancing displacing efficiency when the particle size is much smaller than the pore size, so it is necessary to consider the effect of nanoparticles on the multiphase flow process. The unique interfacial functions of nanomaterials allow nanoparticle suspension to invade those inaccessible nonaqueous fluid-saturated areas. These ultra-small nanoparticles have a very high surface-to-volume ratio, and their surfaces can be functionalized and altered to possess additional functions to adapt to different engineering conditions. The displacement mechanism of nanoparticle suspension can mainly be concluded as wettability alteration, reducing interfacial tension, and enhancing disjoining pressure.

4.2.1. Wettability alteration effect

Wettability conditions are significant for better operations and descriptions of the immiscible multiphase displacement efficiency and fluid dynamics in porous media. By changing porous structure wettability, the capillary force may be adjusted to improve the mobilization of the trapped nonaqueous phase. Applying suitable nanoparticle suspension in oil-wet or neutral conditions can change wettability to water-wet and may substantially improve displacement efficiency [94,95,244]. Microfluidic experiments were performed to identify the wettability alteration effect on decreasing defending phase saturation or increasing displacement efficiency [171,199]. The transformation of liquid menisci in porous media, the synergistic effect of nanoparticles, and droplet/bubble can improve the mobility of the oil phase, further enhancing the displacement efficiency [125]. The stabilization caused by the nanoparticle adsorption on other compounds (e.g., the asphaltenes and fines) may also improve displacement efficiency [245,246]. However, some experiments also indicated that severe irreversible damage would be formed by injecting SiO₂ nanoparticle suspension in crude oil-saturated glass microfluidic porous media due to asphaltene-nanoparticle aggregates [123].

4.2.2. Interfacial tension reduction effect

Interfacial tension reduction can increase the capillary number in the displacement, which can improve displacement efficiency [184,247]. In general, the change of wettability and the decrease of interfacial tension coincide, jointly affecting the displacement process. Through

microfluidic structures mimicking pore-throat geometries, the role of nanoparticles in the mobilization of the trapped nonaqueous droplets can be purified. The capillary number and pore–throat geometry are the two dominant parameters determining the trapped oil droplet size in the pore-throat channels. Nanoparticles can increase the capillary number

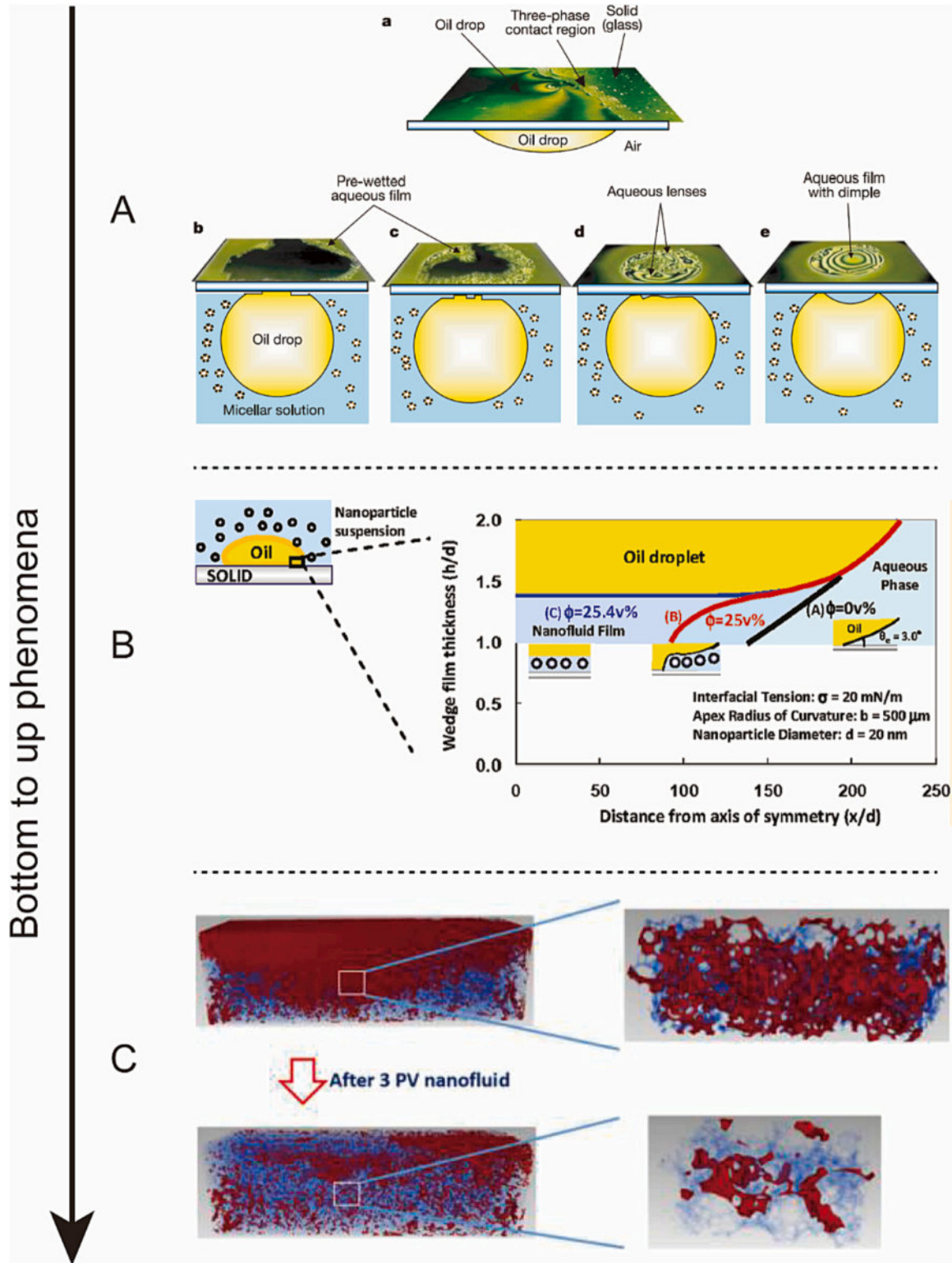


Fig. 17. Bottom to top phenomena of disjoining pressure enhancement effect on displacement performance. (A) Dynamics of the three-phase contact region, a photomicrograph showing the oil drop placed on a glass surface and differential interference patterns formed at the three-phase (solid–liquid–air) contact region. b–e, Photomicrographs taken at increasing times after adding the aqueous micellar solution: b, 30 s; c, 2 min; d, 4 min; and e, 6 min. (B) Effect of the structural disjoining pressure on the meniscus profile. (C) Oil blobs before and after 3 PV nanoparticle suspension flooding at $Ca = 10^{-7}$.

as the weak surfactant, and the nanoparticle concentration is positively related to the droplet mobilization efficiency [208]. It is worthy to note that the interfacial tension decreases as nanoparticle concentration increases and may achieve a promising displacement efficiency, but the higher the particle concentration, the more impairment of porosity and permeability in porous media [121,248].

4.2.3. Disjoining pressure enhancement effect

Suspension-enhanced disjoining pressure has been reported to promote nonaqueous droplet removal from the solid surface in the presence of a micellar solution based on microscopic experimental observation [249]. Two distinct contact lines were captured directly, the outer contact line corresponds to the macroscopic contact angle, and the inner contact line is related to aqueous fluid film spreading. When an air bubble/oil droplet is placed under the lower surface of a hydrophilic glass immersed in concentrated nanoparticle suspension, the bubble/droplet can be detached, driven by the structural disjoining pressure [104] (Fig. 17A). In the wedge region between the bulk suspension where particles move randomly and the film region where exists no particles, particles tend to form the 2D colloidal crystal-like structure where the particle displacement due to Brownian motion is highly inhibited. The particle stratification and corresponding film thickness variation were observed, and the film structural energy isotherm was calculated quantitatively for the film-meniscus microscopic contact angle measurement based on the experimental data [250]. The droplet size decrease will lead to an increase in film stability and film thickness.

The static and dynamic analysis of the wetting and spreading process on solid surfaces has been developed to predict the droplet removal process via nanoparticle suspensions. In the static analysis [251,252], the equilibrium meniscus profiles can be calculated based on the Young-Laplace equation and augmented Young-Laplace equation involving structural disjoining pressure (Fig. 17B). As the volume concentration increased and particle size decreased, the wedge profile deformed further and became parallel to the solid surface, thus achieving spreading phenomena even at a nonzero contact angle. The pressure gradient and system parameters, such as equilibrium contact angle and capillary and hydrostatic pressures, will highly influence the development of the contact line. The threshold values of these parameters in affecting the spreading phenomena of nanoparticle suspension have been demonstrated based on experiments, which further validated these theoretical analyses [252]. Experimental observations of the dynamic spreading process can also be analyzed to elucidate the impact of particle concentration and oil drop volume on the advancing speed of the inner contact line [253]. Based on the governing equation of the fluid dynamics in the wedge film region and the lubrication theory, the expression of inner contact line velocity can be obtained by fitting simulation results and compared with corrected experimental data [254,255].

The relationship between the microscopic wetting/spreading analysis and the macroscopic applications of improving displacement efficiency has also been explored [256]. The underlying mechanism based on the structural disjoining pressure was verified by visualization of the crude oil displacement from the solid substrate, and displacement experiments showed that a polymeric nanoparticle suspension could realize more than 30% incremental displacement efficiency compared to brine based on a glass bead packed model visualized using X-ray micro-CT [256,257]. The additional displacement efficiency decreased as the capillary number increased due to insufficient time for film advancing through structural disjoining pressure at higher capillary numbers [257]. Nanoparticle suspension could significantly change the oil phase distribution and break the large structures into small disconnected oil blobs, indicating the disjoining pressure enhancement effect of suspension on aqueous fluid spreading phenomena (Fig. 17C). Fractured porous media made by sintering glass beads around a dissolvable substrate was applied to investigate the performance of nanoparticle suspension in heterogeneous porous media [258]. These displacement

experiments provided sufficient evidence for the film spreading driven by structural disjoining pressure to improve displacement efficiency. An additional 23.8% oil was displaced using the nanoparticle suspension under water-wet conditions, while only 6% improvement was achieved under oil-water conditions. Capillarity-driven imbibition will dominate the displacement of oil from the matrix region, and the low flow rate can ensure the nanoparticle-induced film velocity controls in the matrix [256–258].

4.2.4. Discussion

The mechanisms mentioned above of nanoparticle suspension pave the way for the applications of nanoparticle suspensions in optimizing the displacement processes. However, the situations in natural and engineering applications are generally more complex, which challenges the validity of the above mechanisms.

For the wettability alteration effect, understanding the optimal wettability condition for best displacement is the prerequisite for applying the wettability alteration effect of nanoparticle suspension on multiphase displacement performance. The wettability effects on multiphase displacement in porous media have been revealed in many studies [259–265]. A consensus seems to have been primarily reached that displacement efficiency is a nonmonotonic function of the wettability index, i.e., a critical wetting condition could occur, yielding the best displacement. Therefore, using suspensions to alter the wettability from oil-wet or neutral conditions to weakly water-wet benefits displacement efficiency improvement. In contrast, changing the system wettability from weakly water-wet to strongly water-wet may not always help achieve the best displacement. Moreover, accurate critical wettability conditions should be considered more under varying capillary numbers, surface roughness values, and viscosity mismatch levels, which may affect the operation or stratagem of suspension application in multiphase displacement [199].

For the interfacial tension reduction effect, the coupling effect of nanoparticle adsorption reducing interfacial tension and the interfacial tension gradient driving nanoparticle interfacial self-assembly may also affect multiphase flow behavior in multiphase displacement. Experiments observed that nanoparticles could easily be transferred from one interface with low interfacial tension to the other with relatively high interfacial tension [92]. Marangoni effect-driven transfer and compression of nanoparticles at new fluid–fluid interfaces may contribute to unique oil remobilization phenomena [91,92]. Dynamic nanoparticle adsorption and corresponding interfacial tension variation are important to the multiphase displacement consequences.

The effectiveness of the surfactant as wettability and interfacial tension modifier could be improved by adding nanoparticles with lower concentrations, which can significantly change the wettability of the sandstone cores from an oil-wet to a water-wet condition [244]. The addition of nanoparticles can reduce the loss of surfactants by adsorption onto the solid surface, which is one of the major concerns that reduce the efficiency of the surfactant flooding process [242,266]. The synergistic effects of nanoparticles and surfactants were observed and evaluated by microfluidic experiments. For example, increasing viscosity by aggregating nanoparticles through the surfactant micelles and decreasing the contact angle by adsorption could mobilize the nonaqueous phase and increase the sweeping ability [243]. Emulsions stabilized by nanoparticles and surfactant mixture show a denser droplet packing in high-permeability layers than stabilized surfactants only, showing a strong diversion effect in heterogeneous channels [195].

For the disjoining pressure enhancement effect, structural disjoining pressure induced by particle ordering in the confined three-phase contact region can highly change the wetting behavior of the aqueous phase and promote the film spreading and non-aqueous phase detachment from the solid surface. However, the applicability and limitations of the structural disjoining pressure theory should be carefully evaluated when applying it to explain displacement improvement effects. (i) The suspension system is assumed to be composed of a pair of symmetry

spherical surfaces surrounded by dispersed hard spheres, some critical parameters such as interfacial properties, wettability conditions, and physical and chemical properties of particle surfaces are ignored in the above derivation of structural disjoining pressure [106]. (ii) The effective particle concentration and the effective particle size are two key parameters that involve the EDL effect on the geometric values [250]. A slight decrease in concentration and increase in particle size may result in a significant change in the magnitude of structural disjoining pressure, as shown in Fig. 7C. In these cases, the bulk volume fraction of nanoparticles usually should be larger than at least 10 vol%, which can maintain the premise of particle ordering in the meniscus region with a sufficient number of particles [108]. However, such a high particle concentration is almost impractical for most experimental and field conditions [267]. (iii) Application conditions should also be carefully evaluated when considering the structural disjoining pressure effect. Most microscopic film spreading experiments and static/dynamic analysis were conducted under a super-hydrophilic condition ($<5^\circ$) with an ultra-low interfacial tension (<1 mN/m) [250,252–256], which is favorable for the contact line movement driven by structural disjoining pressure. However, the structural disjoining pressure effect may be ignorable for neutral or oil-wet conditions and high capillary pressure conditions. (iv) Particle polydispersity should be strictly controlled since polydispersity will lead to dislocations inside the ordering structure and decrease the film stability [108,256]. It was indicated that a 25% polydispersity could lead to a drastic decrease in the magnitude of the interaction force [268]. However, a low polydispersity is hard to achieve for the most commonly used nanoparticle suspensions, especially in harsh underground conditions.

In addition to the displacement mechanism mentioned above, the nanoparticle suspension can also produce unique interface phenomena and enhance the displacement effect under certain circumstances. For example, the oil-in-water emulsion will be generated and stabilized by silica nanoparticles under high flow rates, which generally work with other interfacial phenomena, such as wettability alteration and interfacial tension reduction, to improve displacement efficiency [269]. Functionalized carbon nanotubes promote the formation of water-in-oil emulsions and oil-in-water droplets in the porous medium [270]. The signature generation and growth of tiny water droplets inside the crude oil via negatively charged silica nanoparticle suspension were observed in the glass micromodel [119]. This emulsification phenomenon can enhance the sweeping ability to improve the displacement efficiency [119,269–271]. However, the extent of spontaneous emulsification is closely related to the oil composition and environmental conditions. This effect may be weak for pure model oil, such as decane. Moreover, it may be hard to realize emulsification due to an ultra-low injection velocity (Ca and $Re << 1$).

5. Conclusions and outlook

This paper provides a brief review of multiphase displacement mechanisms controlled by micro/nanoparticle suspension via microfluidic experiments, including fundamentals of suspensions, fabrication/design of microfluidic chips, and displacement mechanisms of deformable micro/nanoparticles and rigid nanoparticles. Microfluidics provides a convenient platform for observing, manipulating, and quantifying the suspension-related displacement process in designed porous structures. Various microfluidic experiments have been carried out to consider the suspension effect on multiphase flow from interfacial phenomena to multiphase flow patterns. However, it is still a long way to better comprehend these relatively complex flows in porous media. The coupling of suspension transport behavior and multiphase flow in porous media may yield anomalous and unexpected displacement phenomena. The different flow conditions and particle chemistries can strongly influence the interactions between fluid, particles, and the porous medium, eventually determining the flow patterns and displacement efficiency.

Although many microfluidic studies on the suspension-related displacement process revealed some basic multiphase displacement mechanisms [26,272], numerous restrictions still exist. The most critical issue is the parallelized visualization and analysis of particle transport or fluid flow dynamics in porous structures at different spatial and temporal scales. Advanced imaging and microchip fabrication technologies can intensify the authenticity of displacement performance, but it is still inadequate to satisfy the actual demand for many engineering purposes [15,273]. Moreover, the complicated properties of suspensions in the porous structure make multiphase flow patterns hard to predict since the basic particle transport behaviors and multiphase flow dynamics at the interface or pore-scale are unclear [154,274]. Upscaling this interfacial or pore-scale phenomenon to macroscopic flow patterns is essential, but only a few studies have been conducted to elucidate this multiscale phenomenon [52,275]. Therefore, future investigations, quantifications, and analyses of suspension-related displacement mechanisms should be envisaged. A deeper fundamental understanding of suspension-related displacement mechanisms in porous media will pave the way for implementing these microfluidic experiments in real applications, evaluating the displacement efficiency, and optimizing the displacement strategies in various areas such as geological engineering, biotechnology, chemistry engineering, etc.

CRedit authorship contribution statement

Wenhai Lei: Investigation, Writing – original draft. **Xukang Lu:** Validation, Writing – original draft. **Moran Wang:** Conceptualization, Supervision, Writing – review & editing.

Declaration of Competing Interest

The authors declare that they have no known competing financial interests or personal relationships that could have appeared to influence the work reported in this paper.

Data availability

No data was used for the research described in the article.

Acknowledgments

This work is financially supported by the National Key Research and Development Program of China (No. 2019YFA0708704) and the NSF grant of China (No. 12272207, U1837602).

References

- [1] Pak T, Luz LfdL, Tosco T, Costa GSR, Rosa PRR, Archilha NL. Pore-scale investigation of the use of reactive nanoparticles for in situ remediation of contaminated groundwater source. *Proc Natl Acad Sci U S A* 2020;117:13366.
- [2] Huppert HE, Neufeld JA. The fluid mechanics of carbon dioxide sequestration. *Annu Rev Fluid Mech* 2014;46:255–72.
- [3] He L, Lin F, Li X, Sui H, Xu Z. Interfacial sciences in unconventional petroleum production: from fundamentals to applications. *Chem Soc Rev* 2015;44:5446–94.
- [4] Louf J-F, Lu Nancy B, O'Connell Margaret G, Cho HJ, Datta Sujit S. Under pressure: hydrogel swelling in a granular medium. *Sci Adv* 2021;17:3840–7.
- [5] Cybulski O, Garstecki P, Grzybowski BA. Oscillating droplet trains in microfluidic networks and their suppression in blood flow. *Nat Phys* 2019;15:706–13.
- [6] Galliker P, Schneider J, Eghlidi H, Kress S, Sandoghdar V, Poulikakos D. Direct printing of nanostructures by electrostatic autofocussing of ink nanodroplets. *Nat Commun* 2012;3:890.
- [7] Verma A, Stellacci F. Effect of surface properties on nanoparticle–cell interactions. *Small*. 2010;6:12–21.
- [8] Kanti Sen T, Khilar KC. Review on subsurface colloids and colloid-associated contaminant transport in saturated porous media. *Adv Colloid Interface Sci* 2006; 119:71–96.
- [9] Lake LW, Johns R, Rossen B, Pope GA. *Fundamentals of Enhanced Oil Recovery*. Richardson, TX: Society of Petroleum Engineers; 2014.
- [10] Israelachvili JN. *Intermolecular and Surface Forces (Third Edition)*. Boston: Academic Press; 2008.
- [11] Rhodes MJ. *Introduction to Particle Technology*. John Wiley & Sons; 2008.

- [12] Liu F, Wang M. Review of low salinity waterflooding mechanisms: wettability alteration and its impact on oil recovery. *Fuel*. 2020;267:117112.
- [13] Tostado CP, Xu JH, Du AW, Luo GS. Experimental study on dynamic interfacial tension with mixture of SDS-PEG as surfactants in a coflowing microfluidic device. *Langmuir*. 2012;28:3120–8.
- [14] Xie C, Xu K, Mohanty K, Wang M, Balhoff MT. Nonwetting droplet oscillation and displacement by viscoelastic fluids. *Phys Rev Fluids* 2020;5:063301.
- [15] Sinton D. Energy: the microfluidic frontier. *Lab Chip* 2014;14:3127–34.
- [16] Sattari A, Hanafizadeh P, Hoorfar M. Multiphase flow in microfluidics: from droplets and bubbles to the encapsulated structures. *Adv Colloid Interface Sci* 2020;282:102208.
- [17] Stone HA, Stroock AD, Ajdari A. Engineering flows in small devices: microfluidics toward a lab-on-a-chip. *Annu Rev Fluid Mech* 2004;36:381–411.
- [18] Zhong J, Riordon J, Wu TC, Edwards H, Wheeler AR, Pardee K, et al. When robotics met fluidics. *Lab Chip* 2020;20:709–16.
- [19] Zhao B, MacMinn CW, Primmkulov BK, Chen Y, Valocchi AJ, Zhao J, et al. Comprehensive comparison of pore-scale models for multiphase flow in porous media. *Proc Natl Acad Sci U S A* 2019;116:13799.
- [20] Druetta P, Raffa P, Picchioni F. Chemical enhanced oil recovery and the role of chemical product design. *Appl Energy* 2019;252:113480.
- [21] Weber F-A, Voegelin A, Kaegi R, Kretzschmar R. Contaminant mobilization by metallic copper and metal sulphide colloids in flooded soil. *Nat Geosci* 2009;2:267–71.
- [22] Wiesner MR, Grant MC, Hutchins SR. Reduced permeability in groundwater remediation systems: role of mobilized colloids and injected chemicals. *Environ Sci Technol* 1996;30:3184–91.
- [23] Tiraferrri A, Chen KL, Sethi R, Elimelech M. Reduced aggregation and sedimentation of zero-valent iron nanoparticles in the presence of guar gum. *J Colloid Interface Sci* 2008;324:71–9.
- [24] Leng J, Wei M, Bai B. Review of transport mechanisms and numerical simulation studies of preformed particle gel for conformance control. *J Petrol Sci Eng* 2021;206:109051.
- [25] Xu Y, Zhu H, Denduluri A, Ou Y, Erkamp NA, Qi R, et al. Recent advances in microgels: from biomolecules to functionality. *Small*. 2022;n/a:2200180.
- [26] Abdulbaki M, Huh C, Sepehrnoori K, Delshad M, Varavei A. A critical review on use of polymer microgels for conformance control purposes. *J Petrol Sci Eng* 2014;122:741–53.
- [27] Hua Z, Lin M, Guo J, Xu F, Li Z, Li M. Study on plugging performance of cross-linked polymer microspheres with reservoir pores. *J Petrol Sci Eng* 2013;105:70–5.
- [28] Li Z, Zhao T, Lv W, Ma B, Hu Q, Ma X, et al. Nanoscale polyacrylamide copolymer/silica hydrogel microspheres with high compressive strength and satisfactory dispersion stability for efficient profile control and plugging. *Indus Eng Chem Res* 2021;60:10193–202.
- [29] Sotiropoulos NP, Chrysikopoulos CV. Interaction between graphene oxide nanoparticles and quartz sand. *Environ Sci Technol* 2015;49:13413–21.
- [30] Krishnamoorti R. Extracting the benefits of nanotechnology for the oil industry. *J Petrol Tech* 2006;58:24–6.
- [31] Barnaji MJ, Pourafshary P, Rasaie MR. Visual investigation of the effects of clay minerals on enhancement of oil recovery by low salinity water flooding. *Fuel*. 2016;184:826–35.
- [32] Song W, Kovscek AR. Functionalization of micromodels with kaolinite for investigation of low salinity oil-recovery processes. *Lab Chip* 2015;15:3314–25.
- [33] Song W, Kovscek AR. Spontaneous clay Pickering emulsification. *Colloids Surf A Physicochem Eng Asp* 2019;577:158–66.
- [34] Hatchell D, Song W, Daigle H. Examining the role of salinity on the dynamic stability of Pickering emulsions. *J Colloid Interface Sci* 2022;608:2321–9.
- [35] Song W, Kovscek AR. Direct visualization of pore-scale fines migration and formation damage during low-salinity waterflooding. *J Nat Gas Sci Eng* 2016;34:1276–83.
- [36] Lei W, Li Q, Yang H-E, Wu T-J, Wei J, Wang M. Preferential flow control in heterogeneous porous media by concentration-manipulated rheology of microgel particle suspension. *J Petrol Sci Eng* 2022;212:110275.
- [37] Lei W, Lu X, Wu T, Yang H, Wang M. High-performance displacement by microgel-in-oil suspension in heterogeneous porous media: Microscale visualization and quantification. *J Colloid Interface Sci* 2022;627:848–61.
- [38] Li J, Jiang Z, Wang Y, Zheng J, Huang G. Stability, seepage and displacement characteristics of heterogeneous branched-preformed particle gels for enhanced oil recovery. *RSC Adv* 2018;8:4881–9.
- [39] Yao C, Lei G, Gao X, Li L. Controllable preparation, rheology, and plugging property of micron-grade polyacrylamide microspheres as a novel profile control and flooding agent. *J Appl Polym Sci* 2013;130:1124–30.
- [40] Yang H, Shao S, Zhu T, Chen C, Liu S, Zhou B, et al. Shear resistance performance of low elastic polymer microspheres used for conformance control treatment. *J Indust Eng Chem* 2019;79:295–306.
- [41] Chauveteau G, Tabary R, Le Bon C, Renard M, Feng Y, Omari A. In-depth permeability control by adsorption of soft size-controlled microgels. *SPE European Formation Damage Conference*. 2003. SPE-82228-MS.
- [42] Bai B, Li L, Liu Y, Liu H, Wang Z, You C. Preformed particle gel for conformance control: factors affecting its properties and applications. *SPE Reserv Eval Eng* 2007;10:415–22.
- [43] Zhao G, You Q, Tao J, Gu C, Aziz H, Ma L, et al. Preparation and application of a novel phenolic resin dispersed particle gel for in-depth profile control in low permeability reservoirs. *J Petrol Sci Eng* 2018;161:703–14.
- [44] Feuston BP, Garofalini SH. Oligomerization in silica sols. *J Phys Chem* 1990;94:5351–6.
- [45] Mädler L, Kammler HK, Mueller R, Pratsinis SE. Controlled synthesis of nanostructured particles by flame spray pyrolysis. *J Aerosol Sci* 2002;33:369–89.
- [46] Guo C, Jordan JS, Yarger JL, Holland GP. Highly efficient fumed silica nanoparticles for peptide bond formation: converting alanine to alanine anhydride. *ACS Appl Mater Interfaces* 2017;9:17653–61.
- [47] Stankic S, Suman S, Haque F, Vidic J. Pure and multi metal oxide nanoparticles: synthesis, antibacterial and cytotoxic properties. *J Nanobiotechnol* 2016;14:73.
- [48] Luo D, Wang F, Zhu J, Cao F, Liu Y, Li X, et al. Nanofluid of graphene-based amphiphilic Janus nanosheets for tertiary or enhanced oil recovery: high performance at low concentration. *Proc Natl Acad Sci U S A* 2016;113:7711.
- [49] Marcano DC, Kosynkin DV, Berlin JM, Sinititskii A, Sun Z, Slesarev A, et al. Improved synthesis of graphene oxide. *ACS Nano* 2010;4:4806–14.
- [50] Kim J, Cote LJ, Kim F, Yuan W, Shull KR, Huang J. Graphene oxide sheets at interfaces. *J Am Chem Soc* 2010;132:8180–6.
- [51] Moore TL, Rodriguez-Lorenzo L, Hirsch V, Balog S, Urban D, Jud C, et al. Nanoparticle colloidal stability in cell culture media and impact on cellular interactions. *Chem Soc Rev* 2015;44:6287–305.
- [52] Molnar IL, Johnson WP, Gerhard JI, Willson CS, O'Carroll DM. Predicting colloid transport through saturated porous media: a critical review. *Water Resour Res* 2015;51:6804–45.
- [53] Prieve DC, Russel WB. Simplified predictions of Hamaker constants from Lifshitz theory. *J Colloid Interface Sci* 1988;125:1–13.
- [54] Russel WB, Saville DA, Schowalter WR. *Colloidal Dispersions*. Cambridge: Cambridge University Press; 1989.
- [55] Bergström L. Hamaker constants of inorganic materials. *Adv Colloid Interface Sci* 1997;70:125–69.
- [56] Li Y, Sariyer OS, Ramachandran A, Panyukov S, Rubinstein M, Kumacheva E. Universal behavior of hydrogels confined to narrow capillaries. *Sci Rep* 2015;5:17017.
- [57] Hamaker HC. The London—van der Waals attraction between spherical particles. *Physica*. 1937;4:1058–72.
- [58] Derjaguin B. Untersuchungen über die Reibung und Adhäsion, IV. *Kolloid-Zeitschrift* 1934;69:155–64.
- [59] Bhattacharjee S, Chen JY, Elimelech M. DLVO interaction energy between spheroidal particles and a flat surface. *Colloids Surf A Physicochem Eng Asp* 2000;165:143–56.
- [60] Bhattacharjee S, Ko C-H, Elimelech M. DLVO interaction between rough surface. *Langmuir* 1998;14:3365–75.
- [61] Bhattacharjee S, Elimelech M. Surface element integration: a novel technique for evaluation of DLVO interaction between a particle and a flat plate. *J Colloid Interface Sci* 1997;193:273–85.
- [62] Hoek EMV, Agarwal GK. Extended DLVO interactions between spherical particles and rough surfaces. *J Colloid Interface Sci* 2006;298:50–8.
- [63] Tian H, Wang M. Electrokinetic mechanism of wettability alternation at oil-water-rock interface. *Surf Sci Rep* 2017;72:369–91.
- [64] Hogg R, Healy TW, Fuerstenau DW. Mutual coagulation of colloidal dispersions. *Trans Faraday Soc* 1966;62:1638–51.
- [65] Bell GM, Levine S, McCartney LN. Approximate methods of determining the double-layer free energy of interaction between two charged colloidal spheres. *J Colloid Interface Sci* 1970;33:335–59.
- [66] Bhattacharjee S, Elimelech M, Borkovec M. DLVO interaction between colloidal particles: beyond Derjaguin's approximation. *Croatica Chem Acta* 1998;71:883–903.
- [67] Hirasaki GJ. Wettability: fundamentals and surface forces. *SPE Formation Eval* 1991;6:217–26.
- [68] Van Oss CJ, Good RJ, Chaudhury MK. Additive and nonadditive surface tension components and the interpretation of contact angles. *Langmuir*. 1988;4:884–91.
- [69] W DJ, Ludmila B, Emil C, Claudio DV, Lucyna H, Abraham M, et al. Contact angles: history of over 200 years of open questions. *Surface Innov*. 2020;8:3–27.
- [70] Girifalco LA, Good RJ. A theory for the estimation of surface and interfacial energies. I. Derivation and application to interfacial tension. *J Phys Chem* 1957;61:904–9.
- [71] Fowkes FM. Attractive forces at interfaces. *Ind Eng Chem* 1964;56:40–52.
- [72] Edwards SA, Williams DRM. Double layers and interparticle forces in colloid science and biology: analytic results for the effect of ionic dispersion forces. *Phys Rev Lett* 2004;92:248303.
- [73] Wang M, Revil A. Electrochemical charge of silica surfaces at high ionic strength in narrow channels. *J Colloid Interface Sci* 2010;343:381–6.
- [74] Kobayashi M, Juillerat F, Galletto P, Bowen P, Borkovec M. Aggregation and charging of colloidal silica particles: effect of particle size. *Langmuir*. 2005;21:5761–9.
- [75] de Gennes PG. Polymers at an interface; a simplified view. *Adv Colloid Interface Sci* 1987;27:189–209.
- [76] Napper DH. Steric stabilization. *J Colloid Interface Sci* 1977;58:390–407.
- [77] Geisel K, Isa L, Richtering W. Unraveling the 3D localization and deformation of responsive microgels at oil/water interfaces: a step forward in understanding soft emulsion stabilizers. *Langmuir*. 2012;28:15770–6.
- [78] Pelley AJ, Tufenkji N. Effect of particle size and natural organic matter on the migration of nano- and microscale latex particles in saturated porous media. *J Colloid Interface Sci* 2008;321:74–83.
- [79] Jenkins P, Snowden M. Depletion flocculation in colloidal dispersions. *Adv Colloid Interface Sci* 1996;68:57–96.
- [80] Kakati A, Bera A, Al-Yaseri A. A review on advanced nanoparticle-induced polymer flooding for enhanced oil recovery. *Chem Eng Sci* 2022;262:117994.
- [81] Torres O, Andablo-Reyes E, Murray BS, Sarkar A. Emulsion microgel particles as high-performance bio-lubricants. *ACS Appl Mater Interfaces* 2018;10:26893–905.

- [82] Torres O, Murray B, Sarkar A. Emulsion microgel particles: novel encapsulation strategy for lipophilic molecules. *Trends Food Sci Technol* 2016;55:98–108.
- [83] An E, Jeong CB, Cha C, Kim DH, Lee H, Kong H, et al. Fabrication of microgel-in-liposome particles with improved water retention. *Langmuir*. 2012;28:4095–101.
- [84] Manoharan VN. Colloidal spheres confined by liquid droplets: geometry, physics, and physical chemistry. *Solid State Commun* 2006;139:557–61.
- [85] Dommersnes P, Rozynek Z, Mikkelsen A, Castberg R, Kjerstad K, Hersvik K, et al. Active structuring of colloidal armour on liquid drops. *Nat Commun* 2013;4:2066.
- [86] Ngai T, Bon SA. Particle-Stabilized Emulsions and Colloids: Formation and Applications. Royal Society of Chemistry; 2014.
- [87] Levine S, Bowen BD, Partridge SJ. Stabilization of emulsions by fine particles I. Partitioning of particles between continuous phase and oil/water interface. *Colloids Surf* 1989;38:325–43.
- [88] Schmidt S, Liu T, Rütten S, Phan K-H, Möller M, Richtering W. Influence of microgel architecture and oil polarity on stabilization of emulsions by stimuli-sensitive core-shell poly(n-isopropylacrylamide-co-methacrylic acid) microgels: mickering versus Pickering behavior? *Langmuir*. 2011;27:9801–6.
- [89] Monteillet H, Workamp M, Appel J, Kleijn JM, Leermakers FAM, Sprakel J. Ultrastrong anchoring yet barrier-free adsorption of composite microgels at liquid interfaces. *Adv Mater Interfaces* 2014;1:1300121.
- [90] Style RW, Isa L, Dufresne ER. Adsorption of soft particles at fluid interfaces. *Soft Matter* 2015;11:7412–9.
- [91] Sashuk V, Winkler K, Żywociński A, Wojciechowski T, Górecka E, Fialkowski M. Nanoparticles in a capillary trap: dynamic self-assembly at fluid interfaces. *ACS Nano* 2013;7:8833–9.
- [92] Lin X, Fang G, Liu Y, He Y, Wang L, Dong B. Marangoni effect-driven transfer and compression at three-phase interfaces for highly reproducible nanoparticle monolayers. *J Phys Chem Lett* 2020;11:3573–81.
- [93] Dehghan Monfared A, Ghazanfari MH, Jamialahmadi M, Helalizadeh A. Adsorption of silica nanoparticles onto calcite: equilibrium, kinetic, thermodynamic and DLVO analysis. *Chem Eng J* 2015;281:334–44.
- [94] Nwidee LN, Al-Anssari S, Barifcani A, Sarmadivaleh M, Lebedev V, Iglauer S. Nanoparticles influence on wetting behaviour of fractured limestone formation. *J Petrol Sci Eng* 2017;149:782–8.
- [95] Karimi A, Fakhrouiean Z, Bahramian A, Pour Khiabani N, Darabad JB, Azin R, et al. Wettability alteration in carbonates using zirconium oxide nanofluids: EOR implications. *Energy Fuel* 2012;26:1028–36.
- [96] Bizmark N, Schneider J, Priestley Rodney D, Datta Sujit S. Multiscale dynamics of colloidal deposition and erosion in porous media. *Sci Adv*. 2020;6:eabc2530.
- [97] Elimelech M, O'Melia CR. Kinetics of deposition of colloidal particles in porous media. *Environ Sci Technol* 1990;24:1528–36.
- [98] Tufenkji N, Elimelech M. Deviation from the classical colloid filtration theory in the presence of repulsive DLVO interactions. *Langmuir*. 2004;20:10818–28.
- [99] Prakash P, Abdulla AZ, Varma M. Contact force mediated rapid deposition of colloidal microspheres flowing over microstructured barriers. *Langmuir*. 2021;37:6915–22.
- [100] Cassie ABD. Contact angles. *Discuss Faraday Soc* 1948;3:11–6.
- [101] Hejazi V, Moghadam AD, Rohatgi P, Nosonovsky M. Beyond Wenzel and Cassie–Baxter: second-order effects on the wetting of rough surfaces. *Langmuir*. 2014;30:9423–9.
- [102] Sun C, McClure J, Berg S, Mostaghimi P, Armstrong RT. Universal description of wetting on multiscale surfaces using integral geometry. *J Colloid Interface Sci* 2022;608:2330–8.
- [103] Morrow NR. *Interfacial Phenomena in Petroleum Recovery*. CRC Press; 1990.
- [104] Wasan DT, Nikolov AD. Spreading of nanofluids on solids. *Nature*. 2003;423:156.
- [105] Boda D, Chan K-Y, Henderson D, Wasan DT, Nikolov AD. Structure and pressure of a hard sphere fluid in a wedge-shaped cell or meniscus. *Langmuir*. 1999;15:4311–3.
- [106] Trokhymchuk A, Henderson D, Nikolov A, Wasan DT. A simple calculation of structural and depletion forces for fluids/suspensions confined in a film. *Langmuir*. 2001;17:4940–7.
- [107] Pieranski P, Strzelecki L, Pansu B. Thin colloidal crystals. *Phys Rev Lett* 1983;50:900–3.
- [108] Nikolov AD, Wasan DT. Dispersion stability due to structural contributions to the particle interaction as probed by thin liquid film dynamics. *Langmuir*. 1992;8:2985–94.
- [109] Tata BVR, Boda D, Henderson D, Nikolov A, Wasan DT. Structure of charged colloids under a wedge confinement. *Phys Rev E* 2000;62:3875–81.
- [110] Hansen J-P, McDonald IR. *Theory of Simple Liquids: With Applications To Soft Matter*. Academic Press; 2013.
- [111] Carnahan NF, Starling KE. Equation of state for nonattracting rigid spheres. *J Chem Phys* 1969;51:635–6.
- [112] Lee LL. An accurate integral equation theory for hard spheres: role of the zero-separation theorems in the closure relation. *J Chem Phys* 1995;103:9388–96.
- [113] O'Connell MG, Lu NB, Browne CA, Datta SS. Cooperative size sorting of deformable particles in porous media. *Soft Matter* 2019;15:3620–3626.
- [114] Du K, Glogowski E, Emrick T, Russell TP, Dinsmore AD. Adsorption energy of nano- and microparticles at liquid–liquid interfaces. *Langmuir*. 2010;26:12518–22.
- [115] Bizmark N, Ioannidis MA, Henneke DE. Irreversible adsorption-driven assembly of nanoparticles at fluid interfaces revealed by a dynamic surface tension probe. *Langmuir*. 2014;30:710–7.
- [116] Destribats M, Lapeyre V, Wolfs M, Sellier E, Leal-Calderon F, Ravaine V, et al. Soft microgels as Pickering emulsion stabilisers: role of particle deformability. *Soft Matter* 2011;7:7689–98.
- [117] Li Z, Geisel K, Richtering W, Ngai T. Poly(N-isopropylacrylamide) microgels at the oil–water interface: adsorption kinetics. *Soft Matter* 2013;9:9939–46.
- [118] Roustaei A, Moghadasi J, Bagherzadeh H, Shahrabadi A. An experimental investigation of polysilicon nanoparticles' recovery efficiencies through changes in interfacial tension and wettability alteration. In: *SPE International Oilfield Nanotechnology Conference and Exhibition*. Noordwijk, The Netherlands: Society of Petroleum Engineers; 2012. p. 7.
- [119] Xu K, Agrawal D, Darugar Q. Hydrophilic nanoparticle-based enhanced oil recovery: microfluidic investigations on mechanisms. *Energy Fuel* 2018;32:11243–52.
- [120] Binks BP. Particles as surfactants—similarities and differences. *Curr Opin Colloid Interface Sci* 2002;7:21–41.
- [121] Hendraningrat L, Li S, Torsæter O. A coreflood investigation of nanofluid enhanced oil recovery. *J Petrol Sci Eng* 2013;111:128–38.
- [122] Alzobaidi S, Wu P, Da C, Zhang X, Hackbarth J, Angeles T, et al. Effect of surface chemistry of silica nanoparticles on contact angle of oil on calcite surfaces in concentrated brine with divalent ions. *J Colloid Interface Sci* 2021;581:656–68.
- [123] Mohammadlinejad P, Hosseinpour N, Rahmati N, Rasaei MR. Formation damage during oil displacement by aqueous SiO₂ nanofluids in water-wet/oil-wet glass micromodel porous media. *J Petrol Sci Eng* 2019;182:106297.
- [124] Al-Anssari S, Barifcani A, Wang S, Maxim L, Iglauer S. Wettability alteration of oil-wet displacement by silica nanofluid. *J Colloid Interface Sci* 2016;461:435–42.
- [125] Dehghan Monfared A, Ghazanfari MH, Kazemeini M, Jamialahmadi M, Helalizadeh A. Wettability alteration modeling for oil-wet calcite/silica nanoparticle system using surface forces analysis: contribution of DLVO versus non-DLVO interactions. *Indus Eng Chem Res* 2018;57:14482–92.
- [126] Dehghan Monfared A, Ghazanfari MH. Wettability alteration of oil-wet carbonate porous media using silica nanoparticles: electrokinetic characterization. *Indus Eng Chem Res* 2019;58:18601–12.
- [127] Bormashenko EY, Boruvka-Neumann. Wenzel and Cassie–Baxter equations as the transversality conditions for the variational problem of wetting. *Colloids Surf A Physicochem Eng Asp* 2009;345:163–5.
- [128] Wenzel RN. Resistance of solid surfaces to wetting by water. *Ind Eng Chem* 1936;28:988–94.
- [129] Jin J, Wang Y, Nguyen TAH, Bai B, Ding W, Bao M. Morphology and surface chemistry of gas-wetting nanoparticles and their effect on the liquid menisci in porous media. *Indus Eng Chem Res* 2019;58:6747–55.
- [130] Yu H, He Y, Li P, Li S, Zhang T, Rodriguez-Pin E, et al. Flow enhancement of water-based nanoparticle dispersion through microscale sedimentary rocks. *Sci Rep* 2015;5:8702.
- [131] Yang H, Kang W, Wu H, Yu Y, Zhu Z, Wang P, et al. Stability, rheological property and oil-displacement mechanism of a dispersed low-elastic microsphere system for enhanced oil recovery. *RSC Adv* 2017;7:8118–30.
- [132] Yang H, Hu L, Chen C, Gao Y, Tang X, Yin X, et al. Synthesis and plugging behavior of fluorescent polymer microspheres as a kind of conformance control agent in reservoirs. *RSC Adv* 2018;8:10478–88.
- [133] Batchelor GK. The effect of Brownian motion on the bulk stress in a suspension of spherical particles. *J Fluid Mech* 1977;83:97–117.
- [134] Xie C, Lv W, Wang M. Shear-thinning or shear-thickening fluid for better EOR? — A direct pore-scale study. *J Petrol Sci Eng* 2018;161:683–91.
- [135] Hoffman RL. Explanations for the cause of shear thickening in concentrated colloidal suspensions. *J Rheol* 1998;42:111–23.
- [136] Teeuw D, Hesselink FT. Power-law flow and hydrodynamic behaviour of biopolymer solutions in porous media. In: *SPE Oilfield and Geothermal Chemistry Symposium*; 1980.
- [137] Browne CA, Shih A, Datta SS. Pore-scale flow characterization of polymer solutions in microfluidic porous media. *Small*. 2020;16:1903944.
- [138] Einstein A. Eine neue Bestimmung der Moleküldimensionen. *Ann Phys* 1906;324:289–306.
- [139] Ferrini F, Ercolani D, de Cindio B, Nicodemo L, Nicolais L, Ranaudo S. Shear viscosity of settling suspensions. *Rheol Acta* 1979;18:289–96.
- [140] Krieger IM, Dougherty TJ. A mechanism for non-Newtonian flow in suspensions of rigid spheres. *Trans Soc Rheol* 1959;3:137–52.
- [141] Scott GD, Kilgour DM. The density of random close packing of spheres. *J Phys D Appl Phys* 1969;2:863–6.
- [142] Chang C, Powell RL. The rheology of bimodal hard-sphere dispersions. *Phys Fluids* 1994;6:1628–36.
- [143] Chang C, Powell RL. Effect of particle size distributions on the rheology of concentrated bimodal suspensions. *J Rheol* 1994;38:85–98.
- [144] Metin C, Bonnacaze R, Nguyen Q. The viscosity of silica nanoparticle dispersions in permeable media. *SPE Reserv Eval Eng* 2013;16:327–32.
- [145] Binks BP, Philip J, Rodrigues JA. Inversion of silica-stabilized emulsions induced by particle concentration. *Langmuir*. 2005;21:3296–302.
- [146] Yu X, Wang R, Wu Y, Ma Y. The flow behaviors of nanoparticle-stabilized bubbles in microchannel: influence of surface hardening. *AIChE J* 2020;66:e16865.
- [147] Stickel JJ, Powell RL. Fluid mechanics and rheology of dense suspensions. *Annu Rev Fluid Mech* 2005;37:129–49.
- [148] Imqam A, Bai B, Delshad M. Micro-particle gel transport performance through unconsolidated sandstone and its blocking to water flow during conformance control treatments. *Fuel*. 2018;231:479–88.
- [149] Li W, Wang D, Yang W, Song Y. Compressive mechanical properties and microstructure of PVA–HA hydrogels for cartilage repair. *RSC Adv* 2016;6:20166–72.
- [150] Lei W, Xie C, Wu T, Wu X, Wang M. Transport mechanism of deformable microgel particle through micropores with mechanical properties characterized by AFM. *Sci Rep* 2019;9:1453.

- [151] Ren K, Zhou J, Wu H. Materials for microfluidic chip fabrication. *Acc Chem Res* 2013;46:2396–406.
- [152] Karadimitriou NK, Hassanizadeh SM. A review of micromodels and their use in two-phase flow studies. *Vadose Zone J* 2012;11:215–28.
- [153] Gerami A, Alzahid Y, Mostaghimi P, Kashaninejad N, Kazemifar F, Amirian T, et al. Microfluidics for porous systems: fabrication, microscopy and applications. *Transp Porous Media* 2019;130:277–304.
- [154] Singh K, Jung M, Brinkmann M, Seemann R. Capillary-dominated fluid displacement in porous media. *Annu Rev Fluid Mech* 2019;51:429–49.
- [155] Chatenever A, Calhoun Jr JC. Visual examinations of fluid behavior in porous media? Part I. *J Petrol Technol* 1952;4:149–56.
- [156] Mattax CC, Kyte JR. Ever see a water flood? *Oil & Gas J* 1961;59:115–28.
- [157] Davis Jr JA, Jones SC. Displacement mechanisms of micellar solutions. *J Petrol Tech* 1968;20:1415–28.
- [158] Terry SC, Jerman JH, Angell JB. A gas chromatographic air analyzer fabricated on a silicon wafer. *IEEE Trans Electron Devices* 1979;26:1880–6.
- [159] Lenormand R, Zarcone C, Sarr A. Mechanisms of the displacement of one fluid by another in a network of capillary ducts. *J Fluid Mech* 1983;135:337–53.
- [160] Trygstad JC, Ehrlich R, Wardlaw NC. Physical modeling of microscopic rock-pore heterogeneities. In: *SPE Enhanced Oil Recovery Symposium*; 1986. p. SPE-14891-MS.
- [161] Lenormand R, Touboul E, Zarcone C. Numerical models and experiments on immiscible displacements in porous media. *J Fluid Mech* 1988;189:165–87.
- [162] Montemagno CD, Gray WG. Photoluminescent volumetric imaging: a technique for the exploration of multiphase flow and transport in porous media. *Geophys Res Lett* 1995;22:425–8.
- [163] Wan J, Tokunaga TK, Tsang C-F, Bodvarsson GS. Improved glass micromodel methods for studies of flow and transport in fractured porous media. *Water Resour Res* 1996;32:1955–64.
- [164] Rangel-German ER, Kovscek AR. A micromodel investigation of two-phase matrix-fracture transfer mechanisms. *Water Resour Res* 2006;42.
- [165] Kumar Gunda NS, Bera B, Karadimitriou NK, Mitra SK, Hassanizadeh SM. Reservoir-on-a-chip (ROC): a new paradigm in reservoir engineering. *Lab Chip* 2011;11:3785–92.
- [166] Zhang C, Oostrom M, Grate JW, Wietsma TW, Warner MG. Liquid CO₂ displacement of water in a dual-permeability pore network micromodel. *Environ Sci Technol* 2011;45:7581–8.
- [167] Ma K, Lontos R, Conn CA, Hirasaki GJ, Biswal SL. Visualization of improved sweep with foam in heterogeneous porous media using microfluidics. *Soft Matter* 2012;8:10669.
- [168] Karadimitriou NK, Joekarniasar V, Hassanizadeh SM, Kleingeld PJ, Pyrakolte LJ. A novel deep reactive ion etched (DRIE) glass micro-model for two-phase flow experiments. *Lab Chip* 2012;12:3413–8.
- [169] Datta SS, Chiang H, Ramakrishnan TS, Weitz DA. Spatial fluctuations of fluid velocities in flow through a three-dimensional porous medium. *Phys Rev Lett* 2013;111:064501.
- [170] Song W, de Haas TW, Fadaei H, Sinton D. Chip-off-the-old-rock: the study of reservoir-relevant geological processes with real-rock micromodels. *Lab Chip* 2014;14:4382–90.
- [171] Zhao B, MacMinn CW, Juanes R. Wettability control on multiphase flow in patterned microfluidics. *Proc Natl Acad Sci U S A* 2016;113:10251–6.
- [172] Wang W, Chang S, Gizzatov A. Toward reservoir-on-a-chip: fabricating reservoir micromodels by in situ growing calcium carbonate nanocrystals in microfluidic channels. *ACS Appl Mater Interfaces* 2017;9:29380–6.
- [173] Xu K, Liang T, Zhu P, Qi P, Lu J, Huh C, et al. A 2.5-D glass micromodel for investigation of multi-phase flow in porous media. *Lab Chip* 2017;17:640–6.
- [174] Yun W, Ross CM, Roman S, Kovscek AR. Creation of a dual-porosity and dual-depth micromodel for the study of multiphase flow in complex porous media. *Lab Chip* 2017;17:1462–74.
- [175] Mehmani A, Kelly S, Torres-Verdin C, Balhoff M. Capillary trapping following imbibition in porous media: microfluidic quantification of the impact of pore-scale surface roughness. *Water Resour Res* 2019;55:9905–25.
- [176] Lei W, Liu T, Xie C, Yang H, Wu T, Wang M. Enhanced oil recovery mechanism and recovery performance of micro-gel particle suspensions by microfluidic experiments. *Energy Sci Eng* 2020;8:986–98.
- [177] Anbari A, Chien HT, Datta SS, Deng W, Weitz DA, Fan J. Microfluidic model porous media: fabrication and applications. *Small* 2018;17:03575.
- [178] Chomsurin C, Werth CJ. Analysis of pore-scale nonaqueous phase liquid dissolution in etched silicon pore networks. *Water Resour Res* 2003;39:1265.
- [179] Kirby BJ, Hasselbrink Jr EF. Zeta potential of microfluidic substrates: 2. Data for polymers. *Electrophoresis* 2004;25:203–13.
- [180] Kirby BJ, Hasselbrink Jr EF. Zeta potential of microfluidic substrates: 1. Theory, experimental techniques, and effects on separations. *Electrophoresis*. 2004;25:187–202.
- [181] Ladd AJC, Szymczak P. Reactive flows in porous media: challenges in theoretical and numerical methods. *Annu Rev Chem Biomol Eng* 2021;12:543–71.
- [182] Gerami A, Armstrong RT, Johnston B, Warkiani ME, Mosavat N, Mostaghimi P. Coal-on-a-chip: visualizing flow in coal fractures. *Energy Fuel* 2017;31:10393–403.
- [183] Singh K, Scholl H, Brinkmann M, Michiel MD, Scheel M, Herminghaus S, et al. The role of local instabilities in fluid invasion into permeable media. *Sci Rep* 2017;7:444.
- [184] Datta SS, Ramakrishnan TS, Weitz DA. Mobilization of a trapped non-wetting fluid from a three-dimensional porous medium. *Phys Fluids* 2014;26:022002.
- [185] Datta SS, Dupin J-B, Weitz DA. Fluid breakup during simultaneous two-phase flow through a three-dimensional porous medium. *Phys Fluids* 2014;26:062004.
- [186] Ju Y, Gong W, Zheng J. Effects of pore topology on immiscible fluid displacement: pore-scale lattice Boltzmann modelling and experiments using transparent 3D printed models. *Int J Multiphase Flow* 2022;152:104085.
- [187] Ju Y, Gong W, Chang W, Sun M. Effects of pore characteristics on water-oil two-phase displacement in non-homogeneous pore structures: a pore-scale lattice Boltzmann model considering various fluid density ratios. *Int J Eng Sci* 2020;154:103343.
- [188] Gong H, Woolley AT, Nordin GP. 3D printed high density, reversible, chip-to-chip microfluidic interconnects. *Lab Chip* 2018;18.
- [189] Ju Y, Xi C, Zheng J, Gong W, Wu J, Wang S, et al. Study on three-dimensional immiscible water–oil two-phase displacement and trapping in deformed pore structures subjected to varying geostress via in situ computed tomography scanning and additively printed models. *Int J Eng Sci* 2022;171:103615.
- [190] Reynolds CA, Menke H, Andrew M, Blunt MJ, Krevor S. Dynamic fluid connectivity during steady-state multiphase flow in a sandstone. *Proc Natl Acad Sci U S A* 2017;114:8187.
- [191] Zuo L, Zhang C, Falta RW, Benson SM. Micromodel investigations of CO₂ exsolution from carbonated water in sedimentary rocks. *Adv Water Resour* 2013;53:188–97.
- [192] Gao CL, Wegner J, Ganzer L. Real structure micromodels based on reservoir rocks for enhanced oil recovery (EOR) applications. *Lab Chip* 2020;20:2197–208.
- [193] Mejia L, Zhu P, Hyman JD, Mohanty KK, Balhoff MT. Coreflood on a chip: core-scale micromodels for subsurface applications. *Fuel*. 2020;281:118716.
- [194] Chatzis I, Dullien FAL. Dynamic immiscible displacement mechanisms in pore doublets: theory versus experiment. *J Colloid Interface Sci* 1983;91:199–222.
- [195] Xu K, Zhu P, Colon T, Huh C, Balhoff M. A microfluidic investigation of the synergistic effect of nanoparticles and surfactants in macro-emulsion-based enhanced oil recovery. *SPE J* 2017;22:459–69.
- [196] Conn CA, Ma K, Hirasaki GJ, Biswal SL. Visualizing oil displacement with foam in a microfluidic device with permeability contrast. *Lab Chip* 2014;14:3968–77.
- [197] Khoshkalam Y, Khosravi M, Rostami B. Visual investigation of viscous cross-flow during foam injection in a matrix-fracture system. *Phys Fluids* 2019;31:023102.
- [198] Ling B, Oostrom M, Tartakovsky AM, Battiato I. Hydrodynamic dispersion in thin channels with micro-structured porous walls. *Phys Fluids* 2018;30:076601.
- [199] Lei W, Lu X, Liu F, Wang M. Non-monotonic wettability effects on displacement in heterogeneous porous media. *J Fluid Mech* 2022;942:R5.
- [200] Dong M, Chatzis I. The imbibition and flow of a wetting liquid along the corners of a square capillary tube. *J Colloid Interface Sci* 1995;172:278–88.
- [201] Al-Housseiny TT, Tsai PA, Stone HA. Control of interfacial instabilities using flow geometry. *Nat Phys* 2012;8:747–50.
- [202] Reyssat M, Courbin L, Reyssat E, Stone HA. Imbibition in geometries with axial variations. *J Fluid Mech* 2008;615:335–44.
- [203] Yao C, Liu B, Li L, Zhang K, Lei G, Steenhuis TS. Transport and retention behaviors of deformable polyacrylamide microspheres in convergent–divergent microchannels. *Environ Sci Technol* 2020;54:10876–84.
- [204] Xie C, Qi P, Xu K, Xu J, Balhoff MT. Oscillative trapping of a droplet in a converging channel induced by elastic instability. *Phys Rev Lett* 2022;128:054502.
- [205] Broens M, Unsal E. Emulsification kinetics during quasi-miscible flow in dead-end pores. *Adv Water Resour* 2018;113:13–22.
- [206] Shin S, Um E, Sabass B, Ault JT, Rahimi M, Warren PB, et al. Size-dependent control of colloid transport via solute gradients in dead-end channels. *Proc Natl Acad Sci U S A* 2016;113:257.
- [207] Bartels WBB, Mahani H, Berg S, Menezes R, van der Hoeven JA, Fadili A. Oil configuration under high-salinity and low-salinity conditions at pore scale: a parametric investigation by use of a single-channel micromodel. *SPE J* 2017;22:1362–73.
- [208] Xu K, Zhu P, Huh C, Balhoff MT. Microfluidic investigation of nanoparticles' role in mobilizing trapped oil droplets in porous media. *Langmuir*. 2015;31:13673–9.
- [209] Xie C, Lei W, Balhoff MT, Wang M, Chen S. Self-adaptive preferential flow control using displacing fluid with dispersed polymers in heterogeneous porous media. *J Fluid Mech* 2021;906:A10.
- [210] Wang J, Zhang H, Liu H, Zhao W, Liu H, Yao C, et al. Quantification of transportation of deformable gel particles in porous media. In: *SPE Annual Technical Conference and Exhibition*. Society of Petroleum Engineers; 2017.
- [211] Bai B, Liu Y, Coste J-P, Li L. Preformed particle gel for conformance control: transport mechanism through porous media. *SPE Reserv Eval Eng* 2007;10:176–84.
- [212] Yao C, Lei G, Cathles LM, Steenhuis TS. Pore-scale investigation of micron-size polyacrylamide elastic microspheres (MPEMs) transport and retention in saturated porous media. *Environ Sci Technol* 2014;48:5329–35.
- [213] Wyss HM, Blair DL, Morris JF, Stone HA, Weitz DA. Mechanism for clogging of microchannels. *Phys Rev E* 2006;74:061402.
- [214] Li S, Yu H, Li T-D, Chen Z, Deng W, Anbari A, et al. Understanding transport of an elastic, spherical particle through a confining channel. *Appl Phys Lett* 2020;116:103705.
- [215] Wyss HM, Franke T, Mele E, Weitz DA. Capillary micromechanics: measuring the elasticity of microscopic soft objects. *Soft Matter* 2010;6:4550–5.
- [216] Ramachandran V, Fogler HS. Plugging by hydrodynamic bridging during flow of stable colloidal particles within cylindrical pores. *J Fluid Mech* 1999;385:129–56.
- [217] Sharp KV, Adrian RJ. On flow-blocking particle structures in microtubes. *Microfluidics Nanofluidics* 2005;1:376–80.
- [218] Goldsstein GH, Santamarina JC. Suspension extraction through an opening before clogging. *Appl Phys Lett* 2004;85:4535–7.
- [219] Dressaire E, Sauret A. Clogging of microfluidic systems. *Soft Matter* 2017;13:37–48.

- [220] Yodh JS, Spandan V, Mahadevan L. Suspension jams in a leaky microfluidic channel. *Phys Rev Lett* 2020;125:044501.
- [221] Donath A, Kantzas A, Bryant S. Opportunities for particles and particle suspensions to experience enhanced transport in porous media: a review. *Transp Porous Media* 2019;128:459–509.
- [222] Yamada M, Seki M. Hydrodynamic filtration for on-chip particle concentration and classification utilizing microfluidics. *Lab Chip* 2005;5:1233–9.
- [223] Chen C, Packman AI, Gaillard J-F. Pore-scale analysis of permeability reduction resulting from colloid deposition. *Geophys Res Lett* 2008;35.
- [224] Schneider J, Priestley RD, Datta SS. Using colloidal deposition to mobilize immiscible fluids from porous media. *Phys Rev Fluids* 2021;6:014001.
- [225] Pritchett J, Frampton H, Brinkman J, Cheung S, Morgan J, Chang KT, et al. Field Application of a New In-Depth Waterflood Conformance Improvement Tool. In: SPE International Improved Oil Recovery Conference in Asia Pacific. Kuala Lumpur, Malaysia: Society of Petroleum Engineers; 2003.
- [226] Barkman JH, Davidson DH. Measuring water quality and predicting well impairment. *J Petrol Tech* 1972;24:865–73.
- [227] Abrams A. Mud design to minimize rock impairment due to particle invasion. *J Petrol Tech* 1977;29:586–92.
- [228] Dai C, Liu Y, Zou C, You Q, Yang S, Zhao M, et al. Investigation on matching relationship between dispersed particle gel (DPG) and reservoir pore-throats for in-depth profile control. *Fuel*. 2017;207:109–20.
- [229] Chen X, Li Y, Liu Z, Li X, Zhang J, Zhang H. Core- and pore-scale investigation on the migration and plugging of polymer microspheres in a heterogeneous porous media. *J Petrol Sci Eng* 2020;195:107636.
- [230] Zhao S, Pu W. Migration and plugging of polymer microspheres (PMs) in porous media for enhanced oil recovery: experimental studies and empirical correlations. *Colloids Surf A Physicochem Eng Asp* 2020;597:124774.
- [231] Li J, Niu L, Lu X. Migration characteristics and deep profile control mechanism of polymer microspheres in porous media. *Energy Sci Eng* 2019;7:2026–45.
- [232] Shokri H, Kayhani MH, Norouzi M. Nonlinear simulation and linear stability analysis of viscous fingering instability of viscoelastic liquids. *Phys Fluids* 2017; 29:033101.
- [233] Herbert AW, Jackson CP, Lever DA. Coupled groundwater flow and solute transport with fluid density strongly dependent upon concentration. *Water Resour Res* 1988;24:1781–95.
- [234] Tan CT, Homsy GM. Simulation of nonlinear viscous fingering in miscible displacement. *Phys Fluids* 1988;31:1330–8.
- [235] Yuan Q, Zhou X, Zeng F, Knorr KD, Imran M. Investigation of concentration-dependent diffusion on frontal instabilities and mass transfer in homogeneous porous media. *Can J Chem Eng* 2018;96:323–38.
- [236] Kim YW, Yoo JY. Axisymmetric flow focusing of particles in a single microchannel. *Lab Chip* 2009;9:1043–5.
- [237] Guiraud P, Costes J, Bertrand J. Local measurements of fluid and particle velocities in a stirred suspension. *Chem Eng J* 1997;68:75–86.
- [238] Gong Y, Zhang Z, He J. Deformation and stability of core-shell microgels at oil/water interface. *Indus Eng Chem Res* 2017;56:14793–8.
- [239] Gong Y, Wang M, Zhang Z, He J. Microgel evolution at three-phase contact region and associated wettability alteration. *Colloids Surf A Physicochem Eng Asp* 2018; 558:297–302.
- [240] Liu Y, Zou C, Zhou D, Li H, Gao M, Zhao G, et al. Novel chemical flooding system based on dispersed particle gel coupling in-depth profile control and high efficient oil displacement. *Energy Fuel* 2019;33:3123–32.
- [241] Lyu Y, Gu C, Fan X, Tao J, Yao X, Dai C, et al. Interfacial rheology of a novel dispersed particle gel soft heterogeneous combination flooding system at the oil-water interface. *Colloids Surf A Physicochem Eng Asp* 2018;559:23–34.
- [242] Wu Y, Chen W, Dai C, Huang Y, Li H, Zhao M, et al. Reducing surfactant adsorption on rock by silica nanoparticles for enhanced oil recovery. *J Petrol Sci Eng* 2017;153:283–7.
- [243] Cheraghian G, Kiani S, Nassar NN, Alexander S, Barron AR. Silica nanoparticle enhancement in the efficiency of surfactant flooding of heavy oil in a glass micromodel. *Indus Eng Chem Res* 2017;56:8528–34.
- [244] Giraldo J, Benjumea P, Lopera S, Cortés FB, Ruiz MA. Wettability alteration of sandstone cores by alumina-based nanofluids. *Energy Fuel* 2013;27:3659–65.
- [245] Kazemzadeh Y, Eshraghi SE, Kazemi K, Sourani S, Mehrabi M, Ahmadi Y. Behavior of asphaltene adsorption onto the metal oxide nanoparticle surface and its effect on heavy oil recovery. *indus eng chem res* 2015;54:233–9.
- [246] Habibi A, Ahmadi M, Pourafshary P, Ayatollahi s, Al-Wahaibi Y.. Reduction of fines migration by nanofluids injection: an experimental study. *SPE J* 2012;18: 309–18.
- [247] Lefebvre du Prey EJ. Factors affecting liquid-liquid relative permeabilities of a consolidated porous medium. *Soc Petrol Eng J* 1973;13:39–47.
- [248] Parvazdavani M, Masihi M, Ghazanfari MH. Monitoring the influence of dispersed nano-particles on oil–water relative permeability hysteresis. *J Petrol Sci Eng* 2014;124:222–31.
- [249] Kao RL, Wasan DT, Nikolov AD, Edwards DA. Mechanisms of oil removal from a solid surface in the presence of anionic micellar solutions. *Colloids Surf* 1988;34: 389–98.
- [250] Nikolov A, Kondiparty K, Wasan D. Nanoparticle self-structuring in a nanofluid film spreading on a solid surface. *Langmuir*. 2010;26:7665–70.
- [251] Chengara A, Nikolov AD, Wasan DT, Trokhymchuk A, Henderson D. Spreading of nanofluids driven by the structural disjoining pressure gradient. *J Colloid Interface Sci* 2004;280:192–201.
- [252] Kondiparty K, Nikolov A, Wu S, Wasan D. Wetting and spreading of nanofluids on solid surfaces driven by the structural disjoining pressure: statics analysis and experiments. *Langmuir*. 2011;27:3324–35.
- [253] Kondiparty K, Nikolov AD, Wasan D, Liu KL. Dynamic spreading of nanofluids on solids. Part I: experimental *Langmuir* 2012;28:14618–23.
- [254] Matar OK, Craster RV, Sefiane K. Dynamic spreading of droplets containing nanoparticles. *Phys Rev E* 2007;76:056315.
- [255] Liu K-L, Kondiparty K, Nikolov AD, Wasan D. Dynamic spreading of nanofluids on solids part II: modeling. *Langmuir*. 2012;28:16274–84.
- [256] Zhang H, Nikolov A, Wasan D. Enhanced oil recovery (EOR) using nanoparticle dispersions: underlying mechanism and imbibition experiments. *Energy Fuel* 2014;28:3002–9.
- [257] Zhang H, Ramakrishnan TS, Nikolov A, Wasan D. Enhanced oil recovery driven by nanofilm structural disjoining pressure: flooding experiments and microvisualization. *Energy Fuel* 2016;30:2771–9.
- [258] Zhang H, Ramakrishnan TS, Nikolov A, Wasan D. Enhanced oil displacement by nanofluid's structural disjoining pressure in model fractured porous media. *J Colloid Interface Sci* 2018;511:48–56.
- [259] Amott E. Observations relating to the wettability of porous rock. *Trans AIME* 1959;216:156–62.
- [260] Morrow NR. Wettability and its effect on oil recovery. *J Petrol Tech* 1990;42: 1476–84.
- [261] Jadhunandan PP, Morrow NR. Effect of wettability on waterflood recovery for crude-oil/brine/rock systems. *SPE Reserv Eng* 1995;10:40–6.
- [262] Al-Futaisi A, Patzek TW. Impact of wettability alteration on two-phase flow characteristics of sandstones: A quasi-static description. *Water Resour Res* 2003; 39.
- [263] Valvatne PH, Blunt MJ. Predictive pore-scale modeling of two-phase flow in mixed wet media. *Water Resour Res* 2004;40.
- [264] Chen J, Hirasaki GJ, Flaum M. NMR wettability indices: effect of OBM on wettability and NMR responses. *J Petrol Sci Eng* 2006;52:161–71.
- [265] Gandomkar A, Rahimpour MR. Investigation of low-salinity waterflooding in secondary and tertiary enhanced oil recovery in limestone reservoirs. *Energy Fuel* 2015;29:7781–92.
- [266] Saxena N, Kumar A, Mandal A. Adsorption analysis of natural anionic surfactant for enhanced oil recovery: the role of mineralogy, salinity, alkalinity and nanoparticles. *J Petrol Sci Eng* 2019;173:1264–83.
- [267] Hu Z, Azmi SM, Raza G, Glover PWJ, Wen D. Nanoparticle-assisted waterflooding in Berea sandstones. *Energy Fuel* 2016;30:2791–804.
- [268] Chu XL, Nikolov AD, Wasan DT. Effects of particle size and polydispersity on the depletion and structural forces in colloidal dispersions. *Langmuir*. 1996;12: 5004–10.
- [269] Li S, Hadia NJ, Lau HC, Torsæter O, Stubbs LP, Ng QH. Silica nanoparticles suspension for enhanced oil recovery: stability behavior and flow visualization. In: SPE Europec featured at 80th EAGE Conference and Exhibition. Vol. Day 4 Thu, June 14, 2018; 2018.
- [270] Ghalamizade Elyaderani SM, Jafari A, Razavinezhad J. Experimental investigation of mechanisms in functionalized multiwalled carbon nanotube flooding for enhancing the recovery from heavy-oil reservoirs. *SPE J* 2019;24: 2681–94.
- [271] Zhang Y, Geng J, Liu J, Bai B, He X, Wei M, et al. Direct pore-level visualization and verification of in situ oil-in-water pickering emulsification during polymeric nanogel flooding for EOR in a transparent three-dimensional micromodel. *Langmuir*. 2021;37:13353–64.
- [272] Nikolov A, Wu P, Wasan D. Structure and stability of nanofluid films wetting solids: an overview. *Adv Colloid Interface Sci* 2019;264:1–10.
- [273] Lifton VA. Microfluidics: an enabling screening technology for enhanced oil recovery (EOR). *Lab Chip* 2016;16:1777–96.
- [274] Liu IB, Sharifi-Mood N, Stebe KJ. Capillary assembly of colloids: interactions on planar and curved interfaces. *Annu Rev Condens Matter Phys* 2018;9:283–305.
- [275] Molnar IL, Pensini E, Asad MA, Mitchell CA, Nitsche LC, Pyrak-Nolte LJ, et al. Colloid transport in porous media: a review of classical mechanisms and emerging topics. *Transp Porous Media* 2019;130:129–56.